Published in final edited form as:

*Neuron*. 2023 April 19; 111(8): 1264–1281.e5. doi:10.1016/j.neuron.2023.01.017.

# Brief synaptic inhibition persistently interrupts firing of fast-spiking interneurons

**Simon Chamberland**[1,*], **Erica R. Nebet**[1], **Manuel Valero**[1], **Monica Hanani**[1], **Robert Egger**[2,3], **Samantha B. Larsen**[1], **Katherine W. Eyring**[1], **György Buzsáki**[1,3,4], **Richard W. Tsien**[1,3,5,*]

[1]NYU Neuroscience Institute and Department of Neuroscience and Physiology, NYU Langone Medical Center, New York, NY 10016, USA

[2]NYU Neuroscience Institute and Department of Otolaryngology, NYU Langone Medical Center, New York, NY 10016, USA

[3]Center for Neural Science, New York University, New York, NY 10003, USA

[4]Department of Neurology, Langone Medical Center, New York University, New York, NY, USA

[5]Lead contact

## SUMMARY

Neurons perform input-output operations that integrate synaptic inputs with intrinsic electrical properties; these operations are generally constrained by the brevity of synaptic events. Here, we report that sustained firing of CA1 hippocampal fast-spiking parvalbumin-expressing interneurons (PV-INs) can be persistently interrupted for several hundred milliseconds following brief $GABA_A$R-mediated inhibition *in vitro* and *in vivo*. A single presynaptic neuron could interrupt PV-IN firing, occasionally with a single action potential (AP), and reliably with AP bursts. Experiments and computational modeling reveal that the persistent interruption of firing maintains neurons in a depolarized, quiescent state through a cell-autonomous mechanism. Interrupted PV-INs are strikingly responsive to Schaffer collateral inputs. The persistent interruption of firing provides a disinhibitory circuit mechanism favoring spike generation in CA1 pyramidal cells. Overall, our results demonstrate that neuronal silencing can far outlast brief synaptic inhibition owing to the well-tuned interplay between neurotransmitter release and postsynaptic membrane dynamics, a phenomenon impacting microcircuit function.

## In brief



*Correspondence: simon.chamberland@nyulangone.org (S.C.), richard.tsien@nyulangone.org (R.W.T.).

AUTHOR CONTRIBUTIONS

S.C. and R.W.T. conceived the project. S.C. performed *in vitro* electrophysiological experiments and analyzed the data. M.V. and G.B. designed, performed, and analyzed *in vivo* recordings. E.R.N. and M.H. analyzed neuronal anatomy. M.H. and S.B.L. performed immunohistochemistry experiments. K.W.E. performed pertussis toxin injections. R.E. and S.C. designed the single-compartment model, and S.C. ran simulations. S.C. and R.W.T. wrote the manuscript with input from all authors.

DECLARATION OF INTERESTS

The authors declare no competing interests.

SUPPLEMENTAL INFORMATION

Supplemental information can be found online at https://doi.org/10.1016/j.neuron.2023.01.017.

Fast-spiking interneurons (FSIs) dominate hippocampal circuitry, but how their firing is controlled is not fully understood. Chamberland et al. find that GABAergic inhibition interrupts FSI firing for much longer than the inhibitory conductance itself. A delicate balance of intrinsic excitability mechanisms sustains the interrupted state, disinhibiting CA1 pyramidal neuron targets.

## INTRODUCTION

Synaptic excitation and inhibition drive or prevent action potential (AP) firing to gate neuronal information transfer. Cortical synaptic inhibition is mediated by functionally heterogeneous GABAergic interneurons (INs),[1–3] including fast-spiking (FS) parvalbumin-expressing INs (PV-INs), powerful modulators of neuronal network activity[4–6] and behavior.[7–9] PV-INs represent a minority of neurons in the hippocampus yet provide synaptic inhibition that supports network oscillations critical for memory storage.[10,11] The impact of PV-INs derives from their extensive axonal arborization,[12] their powerful inhibitory connections with postsynaptic targets,[13] and their intrinsic biophysical properties. Depolarization drives PV-INs to fire non-accommodating bouts of high-frequency APs.[14,15] *In vivo*, this rapid AP discharge is phase-locked to ongoing network activity, with bouts of firing interspersed with periods of relative silence.[16,17] Thus, PV-INs appear integral to coordinated neuronal network activity.

Synaptic inhibition arising from other INs is a powerful constraint on the activity of GABAergic INs.[18,19] This net disinhibitory effect enables information processing and storage, as exemplified by the involvement of PV-INs inhibition in associative fear learning.[20,21] Interconnected populations of INs have long been suggested to entrain ensembles of pyramidal (PYR) cells.[22,23] Reciprocal connectivity among PV-INs contributes to the emergence of network activity such as gamma oscillations.[13,24,25] In hippocampal CA1 (cornu ammonis), populations of vasoactive intestinal peptide (VIP)-expressing INs act as disinhibitory neurons, and somatostatin-expressing INs (SST-INs) can synapse onto PV-INs.[26,27] Although key to understanding circuit function, the inhibitory synaptic wiring diagram for PV-INs is incomplete.

Considering that PV-INs assemble in densely interconnected inhibitory networks[12,28,29] and have a resting potential that is depolarized relative to other IN types,[30–32] PV-INs are poised to respond to GABAergic synapses. Although the classical view holds that neuronal input-output transformation happens on the timescale of synaptic activity, evidence from multiple brain regions shows that neuronal firing can be maintained or emerge following stimulus termination,[33–38] thus providing a physiological substrate for operations such as working memory. Yet, whether and how synaptic inhibition can switch neurons between different firing states is largely unexplored.

Here, we discovered a mechanism based on the interplay between inhibitory synaptic transmission and intrinsic membrane properties that prolongs the silent period exhibited by PV-INs in response to minimal synaptic inhibition, a phenomenon we term persistent interruption of firing. Our analysis reveals that the persistent interruption of firing results from an interplay between a D-type $K^+$ current and a $Na^+$ current that work together to

keep PV-INs quiescent yet hyperresponsive. The interruption of firing is a disinhibitory mechanism for CA1-PYR cells.

## RESULTS

### Synaptic inhibition interrupts firing of FSIs

Synaptic inhibition hyperpolarizes the membrane potential relative to the spike threshold, silencing the neuron for a duration dependent on the dynamics of presynaptic release and postsynaptic receptor activation. PV-INs fire APs at high frequency upon depolarization; yet, how other INs affect PV-IN activity remains generally obscure.

We studied how synaptic inhibition controls PV-IN activity in acute hippocampal slices from P17 to P30 mice. PV-INs were depolarized with steady currents sufficient to evoke fast, sustained firing (Figures 1A and 1B). Synaptic inhibition was elicited through optogenetic stimulation of SST-INs in slices from Sst;;Ai32 transgenic mice. SST- and PV-INs represent generally non-overlapping IN populations[3,39–41]; SST-INs form synaptic contacts on PV-INs. Optogenetic stimulation of SST-IN afferents (20 ms light pulse) during sustained PV-IN firing suppressed subsequent firing (Figures 1A–1C), leaving the neuron in a quiescent depolarized state ($V_M$, −36.4 ± 1.1 vs. −66.6 ± 0.6 mV at rest, n = 29; $p < 0.001$). We termed this phenomenon a persistent interruption of firing (or simply an interruption for brevity), in contrast to the brief silencing expected for an IPSP. The same protocol applied to CA1-PYR neurons caused no such interruption (Figures S1A–S1C), even though optogenetic stimulation of SST-INs evoked similar IPSCs and IPSPs in PV-INs and CA1-PYRs (Figures S1D and S1E). Thus, persistent interruption of firing is a selective means for powerfully controlling PV-IN activity.

Persistent interruption of firing was reliably observed with optogenetic intervention (86.1% ± 2.4%, n = 29; Figures 1C and 1D). When interruption of firing was not induced, PV-IN spiking rapidly recovered (Figure 1C, red trace). In interleaved trials, PV-INs continued firing in the absence of optogenetic intervention (Figures 1B, S2A, and S2B). In most PV-INs (17/29 neurons), normal firing sometimes resumed, achieving full recovery of initial firing frequency (before interruption: 76.3 ± 4.2 Hz; after interruption: 72.3 ± 4 Hz, n = 17; p = 0.37, Mann-Whitney U test). The interruption lasted 757 ± 56 ms (n = 29), ~30-fold longer than the optogenetically evoked IPSP (25.4 ± 4.5 ms, n = 29, Figure 1E). Initial firing rate and the likelihood of observing an interruption were not correlated (Figure S1F). The interruption was observed at all temperatures tested (Figures S1G–S1I). However, increasing the depolarizing current by 37.2% ± 3.6% of rheobase (the just-suprathreshold current) (from 301.9 ± 46.9 to 413.4 ± 66.9 pA, n = 3 neurons) abolished the interruption, enabling firing to continue. Briefer light pulses (2 ms) generated fewer APs in SST-INs (Figures S2C–S2E) and interruptions with lower likelihood yet similar duration (Figures S2G–S2I). This abbreviated optogenetic stimulation evoked IPSPs of similar amplitude but shorter duration (Figures S2J and S2K). Increasing intracellular $Cl^-$ to shift $E_{Cl}$ closer to values in PV-INs (52 and −64 mV)[42,43] hardly altered chances of an interruption (Figures S2L and S2M). Thus, similar to hyperpolarizing inhibition, even shunting inhibition[42] sufficed.

Anatomical reconstructions of 23 PV-INs and cluster analysis based on axonal distribution separated recorded neurons into two groups: (1) perisomatic-targeting (PT) cells with axons ramifying in *stratum pyramidale* (Figures 1F and S3A) and (2) dendrite-targeting (DT) cells with axons innervating *strata oriens* and/or *radiatum* (Figures 1F and S3B). All PT (7/7) and DT (16/16) neurons demonstrated firing interruptions, with similar likelihood (PT: 87.1% ± 3.6%; DT: 85.5% ± 4.0%, p = 1.0, Mann-Whitney U test) and duration (PT: 888.6 ± 39.9 ms; DT: 665.3 ± 84.6 ms, p = 0.18, Mann-Whitney U test). Thus, the interruption of firing greatly prolongs the silent interval generated by GABAergic input to both subtypes of PV-INs.

## A single AP at a unitary connection suffices to interrupt firing

In optogenetic experiments, even small IPSPs could interrupt PV-IN firing for hundreds of milliseconds. Because PV-INs receive synaptic inhibition from multiple sources, including PV-INs themselves,[19] we asked which presynaptic neurons need to be recruited and how many presynaptic APs are required to interrupt PV-IN firing.

In paired recordings, we found that firing from a single presynaptic partner was sufficient to interrupt firing in most synaptically connected pairs (14 out of 16 pairs, Figures 2A and 2D). A single AP evoked by a presynaptic partner was sufficient to interrupt PV-INs in a subset of connected pairs (5/11), but with low likelihood (Figures 2B and 2D). A burst of 5 APs at 100 Hz, a physiological pattern for INs,[16,17] was considerably more efficient at interrupting (1 AP: 4.4% ± 2.3%; 5APs: 36.7% ± 7%; n = 10; p < 0.001, Mann-Whitney U test; Figures 2C and 2D). Initiated by a single presynaptic partner, interruptions were less likely but of similar duration as with optogenetic induction (paired recordings: 739 ± 68 ms, n = 12; optogenetics: 757 ± 56 ms, n = 29; p = 0.67, Mann-Whitney U test). In all cases, the postsynaptic neurons had anatomical features consistent with PV-INs (Figures S3A–S3E). For presynaptic PV-INs, some projected their axons to dendritic layers (6/10), whereas others innervated the perisomatic region (4/10) (Figures 2A and S3D). With presynaptic SST-INs, axons were projected dendritically (4/4) (Figure S3E).

To clarify synaptic mechanisms, we compared inhibitory currents driving the interruption. Single presynaptic spikes reliably generated large IPSCs in PV-INs (Figure 2E), as expected.[44] Bursts of 5 APs (100 Hz) evoked IPSCs displaying short-term depression ($1^{st}$ IPSC: 40.5 ± 4.7 pA; $5^{th}$ IPSC: 13 ± 1.7 pA; p < 0.0001, n = 13; Figures 2E and 2F) but efficient summation. The train-evoked, summated IPSP waveform had similar peak amplitude (1 AP: 1.5 ± 0.1 mV; 5 APs: 1.7 ± 0.2 mV; p = 0.3, n = 7; Figure 2G) yet strikingly slowed decay kinetics (1 AP: $\tau$ = 13.2 ± 1.3 ms; 5 APs: $\tau$ = 54.1 ± 6.8 ms, p < 0.01, n = 7; Figure 2G), suggesting that extended inhibition and a prolonged return to the depolarized $V_M$ was more efficient in interrupting PV-IN firing.

We next estimated how many SST-INs contribute to the total inhibitory current required to reliably trigger firing interruptions. In voltage-clamped PV-INs, optogenetic stimulation of SST-INs evoked IPSCs of 170.6 ± 42.3 pA (n = 6 neurons; Figures 2H–2J), nearly 5-fold larger than the unitary IPSC amplitude in paired recordings (36.9 ± 6.2 pA, n = 3 synaptically connected pairs; Figures 2I and 2J). The ratio in individual cases averaged

4–5 (Figure 2K). Therefore, recruitment of multiple presynaptic INs supported efficient interruption of PV-INs.

### FSIs *in vivo* can remain silent for an extended duration following brief synaptic inhibition

We sought verification that our findings in acute hippocampal slices extended to persistent interruption of firing via brief synaptic inhibition in the intact brain.

For *in vivo* tests, we combined multisite silicon probe electrophysiological recordings with optogenetic stimulation in freely moving *Sst;;Ai32* mice (Figure 3A).[45] SST-INs were identified by their responsiveness to blue light; other neuronal types were categorized based on AP waveform and discharge rate (Figures 3B–3D). Narrow-waveform INs (NW-INs; Figures 3C and 3D) were classified as putative PV-INs.[46] Optogenetic stimulation of SST-INs silenced PV-INs for intervals extending beyond the blue light stimulus in most trials (Figure 3E, 6 typical NW-INs shown, 1,500 trials each). Silencing duration varied across trials, but in all cells, a subset of trials reached the maximal duration sampled (0.6 s; Figure 3E). By averaging trials in deciles across cells, the lowest (0%–10%), middle (45%–55%) and highest (90%–100%), we confirmed that long-lasting inhibition of PV-INs could occur in all PV-INs sampled (Figure 3F1). Middle decile data demonstrated that the silent period consistently outlasted the optogenetic stimulation (Figure 3F1). Conversely, the lowest decile data showed that PV-INs can also rapidly recover firing following an inhibitory event, whereby the silence duration did not outlast optogenetic stimulation (Figure 3F1). This aligned with our *in vitro* observations, wherein failure to induce the interruption of firing occurred, resulting in only brief silences (Figure 1C, red trace). Indeed, parallel analysis of silent intervals in acute slice recordings showed a qualitatively similar progression, from only brief dips in firing frequency to gradually longer silences (Figure 3F2).

We compared the effects of optogenetically induced inhibition on PV-INs with those on CA1-PYRs and wide-waveform INs (WW-INs). The average silence duration was significantly longer for PV-INs (red) than for other cell types (Figures 3G and 3H). This observation is counter-intuitive; PV-INs' baseline firing rates *in vivo* were higher or no lower (NW-INs: 6.14 ± 3.89 Hz, CA1-PYRs: 1.02 ± 0.64 Hz, WW-INs: 5.21 ± 4.53 Hz (mean ± SD); NW vs. PYR: $p < 0.0001$; NW vs. WW: $p = 0.4495$; ANOVA followed by post hoc Tukey-Kramer). Thus, after synaptic inhibition, PV-INs would be expected to recover their firing at least as fast. Yet, PV-INs were silenced for a consistently longer period than all other neuronal subtypes for all optogenetic stimulus durations sampled (Figure 3I). This difference was starkest for the 100-ms light pulse, consistent with our *in vitro* optogenetic experiments (Figures S2H and S2I) and paired recordings (Figure 2D) showing that stimulus trains were more likely to induce an interruption and long silence. Further analysis of such *in vivo* silence durations revealed that the likelihood of observing long silence periods (>500 ms) upon optogenetic activation of inhibitory afferents significantly exceeded expectations from basal inter-spike intervals (ISIs; Figure 3J, Kruskal-Wallis test, $p < 0.05$). This effect was consistent across all neurons sampled *in vivo* (Figure 3K, left), qualitatively resembling *in vitro* data (Figure 3K, right). Clearly, PV-INs remain silent for extended periods following optogenetic activation of GABAergic afferents, both *in vivo* and in acute slices. Based on the parallels *in vivo* and *in vitro*—dependence on cell type and intensity of GABAergic

input—the simplest interpretation is that the interruption of firing has a similar basis in both settings (Figures 3F1 and 3F2; see discussion). To delineate the mechanisms of the interruption, its variable duration, and why *in vivo* interruptions are generally briefer, we next examined underlying biophysical determinants.

## $GABA_AR$ blockade prevents and postsynaptic hyperpolarization suffices to drive the interruption

We focused on pre- and postsynaptic events required to interrupt PV-INs, starting with rapid GABA release and $GABA_A$ receptor ($GABA_AR$) activation as reasonable possibilities given that optogenetic stimulation and presynaptic neuron firing both generated postsynaptic IPSPs. Alternatively, non-classical neurotransmission might also contribute to the interruption through slow postsynaptic inhibition, shunting effects, or sustained release.

We dissected the synaptic requirements of the interruption using optogenetic stimulation in acute slices for throughput and efficiency. Blockade of $GABA_AR$ with bicuculline fully prevented the interruption of firing in all neurons tested (control: 92.7% ± 4.5% likelihood of interruption; bicuculline: 0% likelihood, n = 6, Figures 4A and 4C). This did not exclude a synergistic action of slow $GABA_BR$ signaling. To test this, we directly blocked $GABA_BR$ with 2 μM CGP-55845 (CGP) but found no loss of the interruption of firing, whereas subsequent bicuculline application completely prevented it (n = 8; Figures S4D and S4E). To test G protein involvement more generally, we used 24 h of pertussis toxin treatment to prevent $G_{i/o}$ signaling[47] but found that PV-INs were still interrupted (Figures S4A–S4C). Therefore, presynaptic GABA release and postsynaptic $GABA_AR$ activation are key intermediates in the interruption of firing.

We asked if $GABA_AR$ activation was essential because of the membrane hyperpolarization it invariably causes. We bypassed $GABA_AR$ by mimicking an IPSP waveform with hyperpolarizing current injection. The inducing current was an incremental IPSC-like waveform with two minimal parameters: an instantaneous step and a ramp recovery, effectively a triangle-shaped mock IPSC (Figure 4B). Superimposing the mock-IPSC waveform on a depolarizing current background caused firing interruptions of duration similar to those driven optogenetically (mock IPSC: 766.1 ± 109.5 ms; optogenetic: 914.9 ± 39.7 ms; p = 0.23; n = 5, paired t test; Figures 4B and 4C). Thus, membrane hyperpolarization suffices to interrupt firing.

We varied the parameters of the mock IPSC to determine whether its amplitude or duration was critical (Figures 4D and 4E). Although no correlation emerged between peak hyperpolarization amplitude and interruption likelihood (Pearson correlation: r = −0.15, p = 0.45; n = 8 neurons; Figure 4D), interruption likelihood grew with the mock-IPSC duration (Pearson correlation: r = 0.68, p < 0.0001; n = 8 neurons; Figure 4E). Thus, slower recovery from hyperpolarization engenders a higher likelihood of interruption with optogenetic stimulation (Figures S2H–S2K), paired recordings (Figures 2D–2G), and mock IPSCs (Figure 4E). In the extreme case of no tapering off of hyperpolarizing current, a square hyperpolarizing pulse, firing was almost never interrupted (n = 10; Figures 4F and 4G). Thus, postsynaptic membrane hyperpolarization alone is sufficient to interrupt PV-IN firing, provided that recovery from hyperpolarization is gradual.

These results suggested that interruption of PV-IN firing might be triggered by any presynaptic IN subtype if it provides synaptic inhibition sufficiently strong and slowly decaying. VIP-INs are known to synapse on other INs in hippocampal CA1, thereby mediating disinhibition.[19,27,48–51] However, optogenetic activation of VIP-INs in the *Vip;;Ai32* model was generally insufficient to trigger the interruption (interruption likelihood: 2.8% ± 1.5%; n = 15; Figures S4G–S4I), unlike in *Sst;;Ai32*. We traced this to differing projections of VIP-INs and SST-INs (Figures S4J–S4L). We probed VIP-INs connectivity to PV-INs using oriens-lacunosum moleculare (OLM) INs in CA1 *stratum oriens*, a well-recognized target[49,50] as a standard. IPSCs were recorded sequentially from neighboring PV-INs and putative OLMs upon optogenetic activation of VIP-INs (Figures S4J–S4L). Blue light-evoked IPSCs were 5-fold smaller in PV-INs (19.4 ± 3.2 pA; n = 12) than in OLM-like INs (116.2 ± 16.4 pA; n = 12; $p < 0.001$; Figure S4L). Thus, limited connectivity explains the inability of CA1 VIP-INs to trigger interruptions of PV-IN firing.

## $K_v1$ blockade prevents firing interruption

Knowing that the interruption of firing is initiated by membrane hyperpolarization followed by slow re-depolarization, we sought insight into the contribution of voltage-dependent membrane conductances. Interrupted neurons cannot undergo complete depolarization block, as firing can ultimately resume. Rather, the state of excitability during the interruption was reflected by the first AP upon resumption of firing, which had a more depolarized take-off potential (pre-int: −35.5 ± 1.1 mV, post-int: −32.2 ± 1.2 mV; $p < 0.001$; n = 14), a slower maximal dV/dt (pre-int: 165 ± 6.3 mV/ms, post-int: 119.3 ± 8.8 mV/ms; $p < 0.001$; n = 14), and a smaller amplitude (preint: 63.4 ± 1.9 mV, post-int: 51.9 ± 2.9 mV; $p < 0.001$; n = 14; Figures 5A–5C). The subsequent APs possessed identical characteristics to the last AP before the interruption (values for the 2$^{nd}$ AP post-int: take-off potential: −36.4 ± 1.2 mV; $p = 0.16$; n = 14; maximal dV/dt: 158.2 ± 8; $p = 0.15$; n = 14; amplitude: 63.5 ± 2.8 mV; $p = 0.98$; n = 14; Figures 5A–5C). These features indicate less sodium channel availability during the first spike relative to subsequent spikes.

We derived further clues about the delicate balance of postsynaptic conductances in the quiescent state by examining the $V_M$ trajectory. During the interruption, all $V_M$ recordings demonstrated a small, slow, progressive membrane depolarization with slope averaging 1.7 ± 0.3 mV/s (n = 28, Figure 5D). The gradual depolarization could result from progressive growth of persistent sodium current ($I_{NaP}$), or gradual decline of outward potassium current. D-type $K^+$ currents ($I_D$) mediated by the $K_v1$ channel family generate a gradually inactivating outward current. Indeed, examination of published data revealed that PV-INs express $K_v1$-encoding transcripts,[52] of varying abundance (Figure S5A), notably *Kcna1* and *Kcna2*. Using immunohistochemistry, we verified that PV-INs near CA1 stratum PYR expressed $K_v1.1$ (Figure 5E), with prominent somatic immunoreactivity. Functional involvement of $K_v1.1$ was tested through exposure to dendrotoxin-I (DTX-I, 50 nM), which blocks $K_v1.1$, $K_v1.2$, and $K_v1.6$, or dendrotoxin-K (DTX-K, 50 nM), which selectively blocks $K_v1.1$. Application of either DTX-I or DTX-K prevented the interruption, limiting the quiescent period to that observed in trials where no interruption was induced (Figures 1C, 5F, and 5G). DTX application also increased AP firing rate (Figure S5B), driven in part by a hyperpolarizing shift of AP take-off potential without changes in other parameters

(Figure S5C, see legend). To avoid potential confounding effects of increased firing with DTX, we re-adjusted the depolarizing step size to maintain AP frequency similar to control (Figures 5F and 5G). Nonetheless, DTX reduced the interruption likelihood from 92.5% ± 2.1% in control to 15.5% ± 4.9% in DTX (n = 9, including full abolition in 3/9 neurons; $p < 0.0001$) and abolished the slowly developing depolarization (control: 0.87 ± 0.2 mV/s; DTX-I/K: 0.13 ± 0.06 mV/s; $p < 0.05$; n = 5; Figure 5G, inset).

$K_v1$ channels are heteromultimers incorporating four pore-forming subunits, sometimes including $K_v1.2$ and $K_v1.3$. In tests of involvement of $K_v1.2$ and of $K_v1.3$, exposing neurons to K-Conotoxin RIIIK ($K_v1.2$ blocker) decreased interruption likelihood (Figure S5D), whereas Agitoxin-2 ($K_v1.3$ blocker) did not (Figure S5E). Our results indicated that the interruption relies on $K_v1.1$-containing channels, some possibly containing $K_v1.2$ as well. Finding a crucial role for $K_v1.1$ in the interruption fits with previous findings that $K_v1.1$ inactivation helps control spike timing in neocortical FS-INs.[53]

## $I_D$ and $I_{NaP}$ cooperate to create a drifting stable point in membrane potential

To understand how $K_v1.1$-mediated currents contribute to the interruption, we dissected the membrane current components evoked by depolarization and interrogated their dynamics during the interruption.

PV-INs held under voltage clamp were ramp depolarized from −60 to 0 mV over 2 s (Figure 6A), and currents were recorded in the control solution during exposure to TTX and upon further application of DTX-K. Successive traces were then subtracted to yield the TTX-sensitive current ($I_{TTX\text{-}s}$, current carried by $Na^+$ channels or dependent on $Na^+$ entry) and the DTX-K-sensitive current ($I_{DTX\text{-}s}$, mostly $K_v1.1$ current) (Figure 6B). The pooled I-V relationships of $I_{TTX\text{-}s}$ and $I_{DTX\text{-}s}$ (Figure 6C) were consistently non-linear; their summation (net $I_{TTX\text{-}s}$ + $I_{DTX\text{-}s}$ current, blue trace; Figure 6C) crossed the zero-current axis with a positive slope. This suggested the possibility of a stable point in $V_M$ where inward $I_{TTX\text{-}s}$ and outward $I_{DTX\text{-}s}$ balance each other. Two predictions can be tested during the interruption: first, membrane conductance should be elevated; second, small perturbations to $V_M$ should be followed by rebounding back to the previous level. To verify these predictions, we injected small (50 pA) hyperpolarizing current pulses during the interruption and 2 s later, after recovery of the resting $V_M$ (Figure 6D). Indeed, input resistance during the interruption was lower than its basal value, consistent with the first prediction (Figures 6E and 6F). Furthermore, cessation of the current pulse was followed by rebound depolarization back to the original quiescent level (or rebound hyperpolarization, not shown), indicating an underlying stable point (Figure 6E). Thus, the interruption is a shunted quiescent state, corresponding to an attractor point in $V_M$, arising from interplay between elevated $I_{DTx\text{-}s}$ and $I_{TTX\text{-}s}$. The involvement of inactivating $K^+$ conductance harkens back to the regulation of rhythmic AP firing by $I_A$,[53–57] but here the initiating event is a synaptic input rather than the afterhyperpolarization (AHP) following a spike.

## The firing interruption maintains PV-INs in a hyperresponsive state

PV-INs are more responsive to synaptic recruitment than other elements of feedforward circuits.[58] This makes it interesting to determine how the interruption alters PV-IN

responsiveness to incoming synaptic inputs. The outcome is uncertain because opposing factors are at play: on the one hand, elevated membrane conductance and a lowered driving force for glutamate-induced current should dampen synaptic responsiveness in the quiescent state. On the other hand, sodium channel activation should be enhanced at the depolarized $V_M$ of the interruption, possibly promoting excitability.

EPSPs were evoked by electrical stimulation of Schaffer collateral inputs (Figures 6G–6I). At resting $V_M$ (−66.9 mV), the average EPSP amplitude was 6.53 ± 0.78 mV (n = 5), ~3-fold greater than a unitary EPSP of 2 mV,[58,59] as if the excitatory drive came from ~3 CA3-PYRs. These EPSPs had a fast rise time (2.5 ± 0.4 ms, n = 5), which is consistent with previous findings.[58] When stimulation strength was adjusted to evoke mostly subthreshold EPSPs at resting $V_M$, and spikes only rarely (AP probability = 4.7% ± 4.7%, n = 5, Figures 6H and 6I), the same stimulus was much more likely to evoke an AP during the interruption (82.5% ± 10.8%, n = 5; $p < 0.01$; Mann-Whitney U test; Figure 6J). Thus, the interruption increased PV-IN responsivity to incoming excitatory synaptic inputs.

## A minimal PV-IN model captures the interruption of firing and associated elevation in responsiveness

We performed biophysical modeling of PV-INs, guided by experimental observations, to gain mechanistic insight into the interruption and clarify the basis of its properties as a shunted, quiescent yet hyperresponsive state. As a first approach, we used a model of the perisomatic region of the PV-IN to determine whether an interruption of firing could in principle arise from the interplay between intrinsic conductances and an IPSP-like hyperpolarization.

We assembled a minimal single-compartment model of a FS-IN (STAR Methods), which incorporated transient $Na^+$ current ($I_{Na}$), delayed-rectifier $K^+$ current ($I_{KDR}$) and a small leak current ($I_L$), based on Golomb et al.,[60] supplemented by an inactivating $K^+$ conductance ($I_D$) described in CA1 INs.[61] The model-generated realistic trains of APs in response to current injection (Figure 7A). Firing in the model was interrupted by a mock IPSC (Figure 7A1), and eliminating $I_D$ prevented the interruption (Figure 7A2), even when depolarizing current amplitude was adjusted to maintain the same evoked firing rate (Figure 7A3). The model replicated a telling aspect of observed interruptions: upon resumption of firing, the first AP had a smaller amplitude, indicating that sodium channels are partially inactivated (Figure 7A1, inset). Also, a rectangular hyperpolarizing pulse invariably failed to interrupt the model neuron (Figure 7A4), as seen experimentally (Figures 4F and 4G).

The model facilitated exploring the range of parameters, allowing IPSPs to interrupt firing. An inhibitory conductance with an exponential decay was included, and its amplitude and decay time constant were systematically varied to determine pairs of parameters sufficient to interrupt firing (Figure 7B). Smaller IPSPs required a longer decay time for the interruption to occur; the model IPSP parameters leading to an interruption were similar to those measured experimentally (Figure 7B). Also consistent with experiments (Figures S2L and S2M), varying the model $E_{Cl}$ showed that hyperpolarizing and shunting inhibition[42] both sufficed to interrupt firing, whereas depolarizing inhibition did not (Figures S6A and S6B).

We next aimed to reconstruct the hyperresponsiveness observed in experiments (Figure 6). A compound EPSP-IPSP conductance sequence, simulating the empirical outcome of Schaffer collateral stimulation, was introduced at rest or during an interruption (Figure 7C). A subthreshold excitatory conductance at basal $V_M$ became suprathreshold when imposed during the interruption (Figure 7D), an enhancement of excitability consistent over a broad range of stimuli (Figure 7E). Removing the inhibitory conductance from the simulation and leaving only the EPSP triggered the return of non-accommodating firing, verifying that the IPSP component had renewed the interruption (Figure S6C).

The model offered insight into dynamic fluctuations in $I_D$ and $I_{Na}$ during the mock-IPSC decay and subsequent interruption (Figures 7F1–7F3, S6D, and S6E). During the mock-IPSC decay (induction phase), $I_D$ rises to help limit the speed of $V_M$ re-depolarization, thus preventing AP firing (Figure 7F2). During the maintenance phase, $I_D$ inactivates gradually, whereas $I_{Na}$ gradually increases, resulting in a slow but steady membrane depolarization (Figure 7F2). The sluggish depolarization is accompanied by progressive $Na^+$ channel inactivation (decreasing $h$), explaining why interrupted neurons are maintained in a non-firing condition (Figure 7F3). These results indicate that the interplay between $I_D$ and $I_{Na}$ first initiates and then helps maintain the interruption of firing, first by forcing accommodation and second by keeping the neuron depolarized yet quiescent.

How is firing resumed following the interruption? To address this question, we deconstructed two cases: rapid depolarization-induced firing and resumption of spontaneous firing. observed experimentally and in the model. First, an abrupt redepolarization causes AP firing in both experimental recordings (Figure 4F) and modeling (Figure 7A). This was captured in the model wherein stepwise depolarization generated a large and fast transient $I_{Na}$, not elicited by the gradual depolarization of the mock-IPSC decay (Figures 7G and 7H). This prediction was validated experimentally (Figures S7A–S7D), confirming that the abruptness of the depolarizing stimulus is key to generating an $I_{Na}$ sufficiently large to fire a spike and escape the interruption. In a second comparison between experiment and model, we focused on spontaneous resumption of firing. In 17/17 neurons, this was invariably preceded by membrane oscillations, gradually increasing in amplitude (Figures S7E–S7G). The model indicated that $V_M$ oscillations emerged from a mismatch between the faster activation and inactivation kinetics of $I_{Na}$ compared with $I_D$, which created an instability in $V_M$, seen as a limit cycle in a phase-plane plot (Figure S7G).

In both experiments and modeling, lengthening the duration of pre-induction firing strikingly prolonged the interruption (Figures 7I and 7J). The functional relationship (Figure 7J) had a $t_{1/2}$ of ~0.1 s, an additional indication that FS-INs not only support rapid firing but also harbor ionic currents with subsecond dynamics. Modeling based on previous description of the underlying currents, particularly $I_D$,[61] indicated that AP-evoked $I_D$ gradually increased during continuous firing episodes because of growing $I_D$ de-inactivation (Figure 7K, top, middle), driven by the large AHP following every AP (see STAR Methods). Effects of $I_D$ de-inactivation are buffered by countervailing changes in $I_{KDR}$ during the spike train (Figure 7K bottom), largely sparing AP shape; the impact of $I_D$ de-inactivation is only fully revealed during the interruption (Figure 7F2).

### PV-IN interruption during elevated firing episodes powerfully disinhibits CA1-PYR cells

Knowing that extended PV-IN firing episodes are particularly prone to long-lasting interruptions, we examined the responsiveness of the extended PV-IN firing generated physiologically under the neuromodulatory influence of oxytocin, representing multiple neuromodulators that can directly depolarize the $V_M$ to drive rapid PV-IN firing.[62,63] This might render the PV-IN susceptible to long-lasting interruptions but might also elevate firing probability and lead to early termination of the interruption.

Exposure to the selective oxytocin receptor (OXTR) agonist ($Thr^4$,$Gly^7$)-oxytocin (TGOT) during generally subthreshold depolarization increased PV-IN firing rate 10-fold (from 3.5 ± 1.8 to 38.7 ± 12.2 Hz, n = 5, $p < 0.05$; Mann-Whitney U test; Figures 8A and 8B). In the presence of TGOT, optogenetic stimulation interrupted firing with a high likelihood (97.7% ± 2%, n = 4), and silenced PV-INs persistently (821.8 ± 97.2 ms, n = 4; Figures 8A–8C). Thus, neuromodulatory enhancement of PV-IN activity can produce sustained firing episodes that are amenable to long-lasting interruptions of firing by local synaptic inhibition. This provides an intriguing basis for the abrupt switching of PV-INs between sharply contrasting states of firing.

These observations of prolonged periods of PV-IN silence led us to investigate their consequences for the downstream targets of PV-INs—PYR cells. CA1-PYRs can be heavily influenced by the firing of even a single PV-IN.[18] Paired recordings were performed between PV-INs and deep CA1-PYRs (Figure 8D). Out of 65 attempts, 20 presynaptic PV-INs were synaptically connected to deep CA1-PYRs (30.8% connectivity rate). To assess the impact of an interruption, the CA1-PYR was mildly depolarized with current injection (30.5 ± 3.4 pA; n = 6) to allow tonic firing at 1–2 Hz (Figure 8E), typical of CA1-PYR basal firing.[64–66] Meanwhile, the synaptically connected PV-IN was depolarized with steady current injection to drive firing and then suddenly interrupted with a mock IPSC. We observed that CA1-PYR firing was drastically decreased during bouts of PV-IN firing but returned to basal levels as soon as the PV-IN was silenced by an interruption (Figures 8E and 8F). In aggregate (Figure 8F), CA1-PYR firing rose 3-fold during the interruption (1.35 ± 0.2 Hz; n = 6) compared with that during PV-IN firing (0.45 ± 0.2 Hz; n = 6; $p < 0.01$; Figures 8F and 8G). Remarkably, in trials where PV-IN firing subsequently resumed (interruption ceased, Figure 8E, right), the CA1-PYR firing fell to similar levels as observed during initial PV-IN firing (0.54 ± 0.26 Hz; n = 4; $p = 0.77$; Figure 8G) and was significantly lower than during the interruption (n = 4; $p < 0.01$). These results directly demonstrate that interruption of firing in even a single presynaptic PV-IN suffices to elevate the firing of a target CA1-PYR. Thus, the firing interruption is a powerful disinhibitory mechanism for gating circuit information flow.

## DISCUSSION

Our experiments revealed that the apparently robust, non-accommodating FS phenotype of hippocampal PV-INs is in fact a delicate state that can be toggled off by minimal synaptic inhibition, leading PV-INs to operate in a temporarily depolarized yet silent state. Once initiated, the interruption of firing is a cellautonomous condition that renders PV-INs quiescent yet hyperresponsive. In a circuit context, the interruption of PV-INs firing not

only removes their basal inhibition of CA1-PYRs but also potentiates their responses to subsequent synaptic inputs, thus heightening feedforward inhibition on demand.

In our silicon probe recordings in intact animals, optogenetically induced synaptic inhibition caused silencing of PV-INs that could far outlast fast inhibition itself (Figures 3E–3I). The dependence on cell type and intensity of GABAergic input *in vivo* (Figures 3G–3I) bore a striking resemblance to properties of the interruption studied in acute slices, which were also specific to PV-INs and not PYR neurons (Figures S1A–S1C) and highly dependent on the temporal span of inhibition (Figure 2D). The most parsimonious interpretation is that *in vivo* and *in vitro* interruptions are closely related and share common underpinnings. Insights into mechanisms help explain why the silences *in vivo* were generally briefer than interruptions in acute slices. One factor is that interruption duration depends on recent firing history—briefer firing epochs preceding inhibition result in shorter interruptions afterward—and the uncontrolled periods of PV-IN firing *in vivo* were short-lived compared with the long bursts we imposed for biophysical analysis *in vitro*. A second factor is that fiber-optic-delivered light *in vivo* encounters less favorable geometry and more severe light scattering than illumination of a brain slice; the half-recovery time of firing frequency shrinks steeply with attenuation of the light stimulus as the percentage of successful interruptions gives way to interruption failures (Figure 3L). A third factor is the continual bombardment of PV-INs by excitatory synaptic inputs expected in freely moving animals; if interrupted PV-INs are hypersensitive, those inputs would often trigger early termination of any interruptions. Based on these considerations, we propose that the photo-induced silence *in vivo* (Figure 3F1) aligns, at least qualitatively if not quantitatively, with the more experimentally optimized interruption of firing analyzed *in vitro* (Figure 3F2) and reconstructed *in silico* (Figure 7).

### Synaptic and intrinsic mechanisms controlling the interruption of firing

Both pre- and postsynaptic dynamics contribute to the interruption of firing. GABA release evoked by a single AP from a PV- or SST-IN can occasionally interrupt PV-IN firing, whereas brief bursts of inhibitory input trigger the interruption more reliably. At these synapses, the high release probability, large unitary currents, and mild short-term depression during brief bursts of spikes[13,29,44,67] effectively shape a slow re-depolarizing ramp that is optimal to interrupt PV-INs. Our observations indicate that any form of inhibition can interrupt PV-IN firing if it generates a hyperpolarization that is sufficiently large and slowly decaying.

After $GABA_AR$ conductance has decayed, the interruption is sustained solely by intrinsic mechanisms. The non-accommodating FS pattern of PV-INs is supported by $Na_v1.1$, $Na_v1.6$, and $K_v3$-family channels that enable rapid membrane depolarization and repolarization.[15,68–70] Although these currents are huge, the FS pattern they generate is prone to perturbation by the relatively modest currents provided by brief GABAergic input. Our reconstruction of the interruption splits it into two phases (Figure 7F2). In the first (“induction”) phase, progressive $I_D$ activation slows down the re-depolarization, partially inactivating $I_{Na}$ and, thus forestalling spiking. The second (“maintenance”) phase is sustained by $I_D$ inactivation and gradual $I_{Na}$ activation, pitted against increasing outward current via $I_{KDR}$ (Figures S6D and S6E), to support a slow depolarization that

progressively promotes $I_{Na}$ inactivation, preventing a rebound spike. In PV-INs, $I_D$ was mediated by $K_v1.1$- and $K_v1.2$-containing channels, which, by themselves, demonstrated little inactivation, therefore suggesting that beta subunits are incorporated and help shape the conductance dynamics. Given that $K_v1.1$ is developmentally regulated in the hippocampus, the interruption of firing could be age dependent.[71]

## Impact of persistent interruption of PV-IN firing on the CA1 hippocampal circuit

Intermittent silences would provide FS-INs more time to recover from the high metabolic demands they face[72,73] and would also favor replenishment of depleted presynaptic vesicle pools.[74,75] Further advantages for network function might arise from the concerted silencing of multiple PV-INs by an anatomically divergent presynaptic director. Ensemble silencing would engage a subset of PV-INs as a functional unit. Indeed, multiple place cells in CA1 can undergo coordination by concerted firing of their inhibitory afferents.[76] The monosynaptic inhibitory output from PV-INs provides further divergence, contacting >1,500 CA1-PYRs.[12] Thus, mechanisms regulating the activity of PV-INs will be amplified anatomically, just as the prolongation of GABA-triggered silencing of PV-INs from tens to hundreds of milliseconds would widen any impact of disinhibition.

Our paired recordings of PV-INs and CA1-PYRs explored the consequences of the interruption on information processing in the CA1 circuit. Under conditions mimicking CA1-PYR resting state firing, synaptic inhibition by a single PV-IN decreased CA1-PYR firing rate by ~3-fold. In turn, we demonstrated that shutting off this inhibition by an interruption caused a rapid, powerful and consistent disinhibition of the local PYR neuron activity, an effect fully reversed by resumption of PV-IN firing. In parallel, we also showed that a consequence of the interrupted state is to increase PV-INs responsivity to incoming inputs from the CA3 region, accentuating their potency as feedforward inhibitory elements,[58,77,78] and possibly feedback inhibitory elements as well. Altogether, the CA1 circuit will switch toward local information processing while veering away from receiving external inputs.[79,80]

PV-INs strongly regulate CA1 population activity.[4,81] PV-INs, but not axo-axonic cells, are active during sharp wave ripples (SPW-Rs), high-frequency oscillations associated with memory formation.[1,16,82–84] We speculate that regulating PV-IN firing by mechanisms similar to those found here could help control SPW-R duration, consistent with computational modeling of disinhibitory interactions during SPW-Rs.[85] In turn, the duration of CA1 SPW-Rs affects performance in hippocampal-based learning and memory tasks.[86]

## Possible implications for disinhibition and pattern switching in neocortical systems

In the neocortex, *in vivo* studies have shown that PV-INs can experience intermittent bouts in a depolarized yet silent state close to AP threshold.[31,32] This raises the possibility that the interruption occurs outside the hippocampus and contributes more generally to *in vivo* regulation of PV-INs. In cortical areas, PV-INs are crucial for controlling neuronal network activity[4–6,10,11] and in regulating animal behavior.[7–9] Disinhibition provides a permissive signal that allows input-selective integration by principal neurons.[51,87–89] Inhibition of PV-INs supports learning and memory via downstream disinhibition of principal neurons.[20,21]

Thus, more broadly beyond hippocampal CA1, the interruption of PV-IN firing and its net disinhibitory effect could participate in functions such as associative learning and spatially guided reward learning.[20,51]

The persistent interruption of firing can be compared with forms of persistent activity invoked to explain higher-order phenomena such as working memory and memory formation.[33,90,91] The initiation of persistent activity can be cell-autonomous,[33,34,92–95] sometimes reflecting integration of previous activity.[33,93] In other cases, the maintenance of persistent activity requires continual neuromodulatory input,[33,34,92] engagement of other circuit elements,[36,91] or participation of nearby astrocytes.[96] In contrast, the firing interruption of PV-INs, while induced in a circuit context, is demonstrably sustained in a cell-autonomous manner. It is the first demonstration of switch-like changes in persistent firing activity initiated by a single presynaptic partner. Nonetheless, this simple flip-flopping between full-throated spiking and no firing could be an interactive building block of more complex circuit phenomena, incorporating neuromodulation, competing groups of neurons, non-neuronal partners, and switching following the integration of seconds-long trains of activity.[33,34]

### Cooperation between persistent interruption of firing and slow neuromodulation

The interruption mechanism throws a new light on slowly acting neuromodulation. Oxytocin exemplifies agents that alter the intrinsic properties of PV-INs and drive them to fire rapidly and steadily. This provides a condition favoring the interruption; PV-INs then become hypersensitive as a result of the interruption, sometimes resulting in subthreshold synaptic inputs at rest transforming to suprathreshold. In this neuromodulatory setting, the firing interruption can relieve principal neurons from inhibition within milliseconds (Figures 8D–8G). We interpret the “on” and “off” of the interruption as complementary ways of sharpening up the temporal contrast between adjoining states of firing rate rather than merely raising or lowering the mean firing rate. This contrast enhancement can occur following brief or long epochs of PV-IN firing—the duration of the disinhibitory window will be a function of the pre-interruption PV-IN firing duration (Figures 7I–7K). The sharp transition would provide the kind of rapid disinhibitory switch invoked by Shen et al. to impose winner-take-all dynamics in a decision-making circuit.[97] This disinhibitory scenario complements a distinct mechanism wherein spontaneous firing of PV-INs acts over many seconds to fatigue GABAergic synapses and thus weaken feedforward inhibition.[62,98] The common feature is an interplay between slow neuromodulators and fast GABAergic transmission that causes a net disinhibition of principal neurons. Such disinhibition could enable CA1-PYRs to generate dendritic plateaus and potentially favor synaptic plasticity and place field formation.[99]

## STAR★METHODS

### RESOURCE AVAILABILITY

**Lead contact—**Further information and requests for resources and reagents should be directed to and will be fulfilled by the lead contact, Richard W. Tsien (richard.tsien@nyulangone.org).

**Materials availability—**This study did not generate new unique reagents.

**Data and code availability—**The datasets generated in the current study are available from the lead contact on reasonable request.

The *in vivo* data for this study is publicly available in the Buzsáki Lab Databank: https://buzsakilab.com/wp/public-data/.

All custom code for preprocessing and analyzing the *in vivo* data can be found on https://github.com/valegarman/HippoCookBook (Zenodo: 6902376; https://doi.org/10.5281/zenodo.6902376). All original code has been deposited at Zenodo and is publicly available as of the date of publication. DOIs are listed in the key resources table.

## EXPERIMENTAL MODEL AND SUBJECT DETAILS

**Animals—**All experiments involving animals were approved by the Institutional Animal Care and Use Committee (IACUC) at New York University Langone Medical Center. For *in vitro* experiments, wild-type (C57BL/6) and transgenic mice (P17 – P30) of either sex were used indiscriminately in this study. For interneuron recordings in slices, homozygous Pv-Cre (Jackson Labs; Stock No. 008069) or Sst-IRES-Cre (Jackson Labs; Stock No. 013044) mice were crossed with homozygous Ai9 mice (Jackson Labs; Stock No. 007909) to generate Pv;;Ai9 and Sst;;Ai9 animals which demonstrated strong Td-Tomato expression in PV- or SST-expressing INs. For optogenetic stimulation of SST-expressing INs, homozygous Sst-IRES-Cre or Vip-IRES-Cre mice (Jackson Labs: Stock No. 010908) were crossed with homozygous Ai32 mice (Jackson Labs; Stock No. 024109). This cross resulted in offspring with channelrhodopsin-2(H134R) (abbreviated as ChR2 in figures) expression in SST- or VIP-expressing INs (*Sst;;Ai32 or Vip;;Ai32*). Animals from the same strains were used for *in vivo* and *in vitro* experiments. For *in vivo* experiments, 2 *Sst;;Ai32* mice (28–35 gr, 4–6 months old) were used. Potential confounding factors in our experiments include the use of SST-Cre animals crossed with the Ai32 reporter line to provide optogenetic access to this population of GABAergic cells. We note that the SST-Cre model is imperfect and can target PV-INs, possibly explained by non-selective Cre-recombinase expression or the fact that the SST and PV population of neurons show some overlap in the CA1 hippocampus.[101,102]

## METHOD DETAILS

**Acute hippocampal slice preparation—**Acute hippocampal slices (300 μm) were prepared by deeply anesthetizing animals with isoflurane. The brain was rapidly extracted and placed in ice-cold slicing solution, containing (in mM): 185 sucrose, 25 $NaHCO_3$, 2.5 KCl, 25 glucose, 1.25 $NaH_2PO_4$, 10 $MgCl_2$, 0.5 $CaCl_2$; pH 7.4, 330 mOsm. This solution was continuously oxygenated with a 95% $O_2$ and 5% $CO_2$ mixture. The brain was dissected, and slices were cut on a Leica VT1000 S Vibrating blade microtome. Slices were transferred to heated (32°C) slicing solution for 30 minutes, after which slices were transferred to oxygenated artificial cerebrospinal fluid (ACSF), containing (in mM): 125 NaCl, 25 $NaHCO_3$, 2.5 KCl, 10 glucose, 2 $CaCl_2$, 2 $MgCl_2$; pH 7.4, 300 mOsm. Slices were left in this solution at room temperature for the duration of the experiment.

***In vitro* electrophysiological recordings—**Acute slices were transferred to a recording chamber and held under a nylon mesh. The preparation was continuously perfused with oxygenated ACSF (2 ml/min) at room temperature (20 ± 2C, mean ± SD), unless otherwise indicated (Figures S1H and S1I: 31.3 ± 0.9C, mean ± SD). Recording electrodes were prepared from borosilicate filaments (TW150–4, World Precision Instruments) on a P-97 Sutter Instrument micropipette puller and had a resistance of 3 – 6 MΩ. For paired recordings, experiments were performed under an upright microscope (BX50WI, Olympus) equipped with a 40X objective. Whole-cell recordings were sequentially obtained by first bringing both recording electrodes (MP-285 micromanipulators, Sutter Instrument) close to targeted neurons and then forming giga-seals. For paired whole-cell electrophysiological recordings presented in Figures 2 and 8, experiments were performed with a MultiClamp 700B amplifier and digitized at 10 kHz with a Digidata 1322A. Data was sent to a PC and acquired with the Clampex 9.2 software. All other electrophysiological recordings were performed with an upright microscope (BX61WI, Olympus) equipped with a 40X objective. The electrophysiological signal was amplified with an Axopatch 200B, digitized at 10 kHz (Digidata 1322A) and recorded on a PC equipped with the Clampex 8.2 software. The intracellular solution contained (in mM): 130 K-gluconate, 10 HEPES, 2 $MgCl_2.6H_2O$, 2 $Mg_2ATP$, 0.3 NaGTP, 7 $Na_2$-Phosphocreatine, 0.6 EGTA, 5 KCl; pH 7.2 and 295 mOsm. Under these conditions, the total intracellular [$Cl^-$] was 9 mM and the theoretical $Cl^-$ reversal potential was −69 mV. In experiments with elevated intracellular [$Cl^-$] reported in Figures S2L and S2M, the intracellular solution contained (in mM): 121.5 K-gluconate, 10 HEPES, 2 $MgCl_2.6H_2O$, 2 $Mg_2ATP$, 0.3 NaGTP, 7 $Na_2$-Phosphocreatine, 0.6 EGTA, 13.5 KCl; pH 7.2 and 295 mOsm. Under these conditions, the total intracellular [$Cl^-$] was 17.5 mM and the theoretical $Cl^-$ reversal potential was −52 mV. Only cells with a series resistance below 25.7 MU were included. Series resistance was 18.12 ± 0.72 MU for current-clamp recordings presented in Figure 1. Series resistance in the voltage-clamp recordings presented in Figures 6A–6C was 19.71 ± 1.68 MU (n = 8) and was not compensated. In current-clamp recordings, traces shown everywhere are raw data not corrected for the voltage drop across the series resistance during current injection. After allowing for an ohmic voltage drop, the AHP consistently hyperpolarized VM below resting. The peak afterhyperpolarization in pooled data ranged from −84.2±0.9 mV ($1^{st}$ AP) to −76.8±1.1 mV ($20^{th}$ AP), consistently negative to resting levels (−65.6±0.6 mV; n=27; p<0.0001 for both comparisons). These results align with simulations indicating the AHP's key role in driving de-inactivation of $I_D$ and induction of the interruption. Schaffer collaterals were stimulated by positioning a tungsten electrode connected to a stimulus isolator (A360, World Precision Instruments) in the stratum radiatum of the CA3 region. Photostimulation of SST-INs was performed with 470 nm light from a light-emitting diode (LED) delivered to the slice with an optical fiber. A TTL signal was sent from the digitizer to an LED controller for precisely timed stimulation (WT&T Inc.). For voltage-clamp recordings, neurons were held at the indicated potential in the figures. The liquid junction potential was not corrected. The following pharmacological reagents were used in this study: tetrodotoxin (1 μM, Sigma), bicuculline (10 μM, Sigma), CGP-55845 (2 μM, Tocris) dendrotoxin-K (50 nM, Alomone), dendrotoxin-I (50 nM, Alomone), K-Conotoxin RIIIK (200 nM, Alomone), Agitoxin-2 (10 nM, Alomone), TGOT ((Thr$^4$,Gly$^7$)-oxytocin, 400 nM, Bachem).

**_In vivo_ electrophysiological recordings and optogenetic stimulation—** *Sst;Ai32* mice were implanted with 64-site silicon probes (NeuroNexus A5x12-16-Buz-lin-5mm-100-200-160-177) in dorsal CA1 (AP 2.0 mm, ML 1.6 mm, DL 1.1 mm). Ground and reference wires were implanted in the skull above the cerebellum, and a grounded copper mesh hat was constructed shielding the probes. Probes were mounted on microdrives that were advanced to pyramidal layer over the course of 5–8 days after surgery. A 100 μm fiber optic was attached to the silicon probe.[45] The back end of the fiber was coupled to a laser diode (450 nm blue, Osram Inc.). Animals were allowed to recover for at least one-week prior to recording. Mice were housed under standard conditions in the animal facility and kept on a 12 h reverse light/dark cycle. Electrophysiological data were acquired using an Intan RHD2000 system (Intan Technologies LLC) digitized with 30 kHz rate. For optogenetic tagging of Sst-expressing neurons, blue laser light (450 nm, Osram Inc) pulses were delivered. The maximum light power at the tip of the optic fiber was 1 to 4 mW. 20, 50 and 100 ms light pulses were delivered (n = 500 – 1000 times at each duration at 400 ± 200 ms random intervals).

**Biocytin revelation, neuronal tracing, and anatomical classification—**Neurons were passively filled with biocytin in the whole-cell configuration. Following recordings, the pipette was carefully retracted, and the acute slice was placed in a petri dish between filter papers. Slices were fixed overnight with 4% PFA in PBS. Biocytin was revealed by treating the slices with Triton (1%) and incubating overnight in an Alexa-633 conjugated streptavidin (1:200, ThermoFisher Scientific). The following day, slices were mounted on microscope slides with ProLong Gold (ThermoFisher Scientific). Images were acquired on a Zeiss confocal system (Axo Imager.Z2). Anatomical tracings were performed in Neurolucida 360 (2.70.1, MBF Bioscience) on a personal computer.

For anatomical classification, the axonal length in the dendritic layers (strata oriens and radiatum) and in the somatic layer (stratum pyramidale) were quantified in Neurolucida. For each cell, axonal length was measured using Neurolucida 360. The axonal length in the somatic or dendritic layers were then normalized to the total axonal length for each cell. Using this dataset, K-means clustering analysis in Python was used to cluster interneurons in two groups.

**Stereotaxic injections—**For stereotaxic surgeries, mice were anesthetized with isofluorane (2%–5%) and secured in a stereotaxic apparatus (Kopf). Glass pipettes (Drummond Scientific) were formed using a P-2000 puller (Sutter Instrument) and were characterized by a long taper and 10–20 μm diameter tips. Pipettes were back-filled with mineral oil (Fisher Scientific) before being loaded with pertussis toxin (Sigma P7208) and positioned over the lateral ventricle (coordinates relative to bregma, in mm: 0.25 lateral, 0.3 anterior, −3 ventral). A small drill hole was made in the skull to allow for pipette insertion. 1–2 μL of 0.1 g/L pertussis toxin were injected unilaterally into the ventricle. Experiments were performed 24–72 hours following injection. Throughout the surgery, body temperature, breathing and heart rate were monitored. Saline was administered subcutaneously (s.c) to maintain hydration and the animal was monitored post-operationally for signs of distress

and discomfort. Buprenorphine (0.1 mg/kg s.c.) was given for analgesia. No major adverse effects of the surgery or pertussis toxin injection were observed.

**Immunohistochemistry—**For localization of $K_V1.1$ in PV-IN, 20 μm thick hippocampal slices from Pv-Ai9 animals were prepared on a cryostat (CM3050 S, Leica). Slices were treated with a $K_v1.1$ recombinant rabbit monoclonal antibody (SN66–06, ThermoFisher Scientific) overnight and with an Alexa-488 conjugated secondary antibody for two hours on the following day. Images were acquired on a Zeiss confocal system (Axo Imager.Z2). Pv-Ai9-expressing interneurons were considered positive for $K_v1.1$ if the Alexa-488 fluorescence intensity at the soma was two standard deviations above the surrounding background.

**Computational modeling—**A conductance-based fast-firing interneuron model was adapted from previously published data presented in ModelDB (senselab.med.yale.edu/modeldb/).[60] The model was implemented in NEURON (version 7.7). The model consisted of a single cylindrical compartment with a diameter of 10 μm and a length of 10 μm. Axial resistance was set to 100 Ωcm, membrane capacitance was set to 1 $\mu F/cm^2$ and the leak conductance was set to $g_{pas} = 0.0001$ $S/cm^2$ with a reversal potential of −65 mV. The model contained a $Na^+$ conductance ($Na_t$; reversal potential: 50 mV; $g_{Na} = 0.1125$ $S/cm^2$) and a delayed-rectifying $K^+$ conductance ($K_{dr}$; reversal potential: −90 mV; $g_{Kdr} = 0.225$ $S/cm^2$)[60] as well as an inactivating $K^+$ conductance ($K_D$).[61] These conductances were modeled using the Hodgkin-Huxley formalism. Parameters of $Na_t$ and $K_{dr}$ were left unchanged. The maximum conductance $G_D$ of the inactivating $K^+$ conductance was empirically determined based on the firing frequency measured experimentally before (77 Hz) and after DTX treatment (90 Hz) and set to 0.01 $S/cm^2$. The time constant of inactivation was slowed 60-fold relative to the interneuron model[60] to roughly approach the slow decay of DTX-sensitive current we observed (Figure S7A). Temperature during simulations was set to 24°C. Excitatory and inhibitory synaptic conductances were modeled with a double-exponential time course of onset and decay. Excitatory currents had rise and decay times of 0.2 ms and 2 ms, a maximum conductance of 0.3 nS, and a reversal potential of 0 mV. Inhibitory currents had rise and decay times of 1 ms and 50 ms, a maximum conductance of 0.6 nS, and a reversal potential of −65 mV. Decay time and maximum conductance of inhibitory synapses were systematically varied to generate Figure 7B. Simulations were performed with a step size of 0.025 ms. Simulations were performed on a personal computer in the NEURON interface controlled by Python and simulated traces were analyzed in Igor Pro 6.37 (Wavemetrics).

## QUANTIFICATION AND STATISTICAL ANALYSIS

**Electrophysiological data analysis—***In vitro* electrophysiological data were analyzed in Clampfit 10.3 (Molecular Devices) and in Igor Pro 6.37 (Wavemetrics). The likelihood of observing a firing interruption was obtained by dividing the number of sweeps showing a successful interruption by the total number of acquired sweeps. An interruption was deemed successful if the silence period exceeded the IPSP duration. The IPSP duration was measured from its initiation to 95% recovery. The interruption duration was measured as the time from the IPSP onset to time of the first AP after firing resumption. For graphs

representing the AP frequency as a function of time, the timing of the AP was determined at its peak amplitude, and the data was binned in 20 ms width.

For *in vivo* electrophysiological data analysis, spike sorting was performed semi-automatically with KiloSort 47 (https://github.com/cortex-lab/KiloSort), using our own pipeline KilosortWrapper (a wrapper for KiloSort, DOI; https://github.com/brendonw1/KilosortWrapper). This was followed by manual adjustment of the waveform clusters using the software Phy2 (https://github.com/kwikteam/phy) and plugins for Phy designed in the laboratory (https://github.com/petersenpeter/phy-plugins). The following parameters were used for the Kilosort clustering: ops.Nfilt: 6 * numberChannels; ops.nt0: 64; ops.whitening: 'full'; ops.nSkipCov: 1; ops.whiteningRange: 64; ops.criterionNoiseChannels: 0.00001; ops.Nrank: 3; ops.nfullpasses: 6; ops.maxFR: 20000; ops.fshigh: 300; ops.ntbuff: 64; ops.scaleproc: 200; ops.Th: [4 10 10]; ops.lam: [5 20 20]; ops.nannealpasses: 4; ops.momentum: 1./[20 800]; ops.shuffle_clusters: 1.

Unit clustering generated three separable groups (Figure 3B) based on their autocorrelograms, waveform characteristics and firing rate. Putative CA1-PYRs, narrow-waveform interneurons and wide-waveform interneurons were tentatively separated based by these three clusters.[103] Definitive cell identity was assigned after inspection of all features, assisted by monosynaptic excitatory and inhibitory interactions between simultaneously recorded, well-isolated units and optogenetic responses. Units were defined as optically tagged using a p value cutoff of $10^{-3}$.[45]

**Statistical Treatment—**For *in vitro* electrophysiological data, Shapiro-Wilk test was performed to test for normality of data distribution. For normally distributed data, a paired or unpaired Student's t-test was performed to evaluate statistical significance. For non-normally distributed data, a Mann-Whitney U test was used where indicated. Pearson rank correlation was used to evaluate correlation between parameters in Figures 4D, 4E, and S1F. A two-way ANOVA was used to evaluate statistical significance in Figure 7J. Experimental groups were deemed significantly different if $p < 0.05$. Statistical tests were performed in Clampfit 10.3 (Molecular Devices) and in Python. Statistical significance is reported on figures as follows: * $p < 0.05$, ** $p < 0.01$, *** $p < 0.001$.

Statistical analyses for *in vivo* electrophysiological data were performed blinded or did not require manual scoring and were performed with standard MATLAB functions. No specific analysis was used to estimate minimal population sample and the number of animals, trials, and recorded cells were similar to those employed in previous works.[45,103] Unless otherwise noted, for all tests, nonparametric two-tailed Wilcoxon's paired signed-rank test and Kruskal-Wallis one-way analysis of variance were used. When parametric tests were used, the data satisfied the criteria for normality (Kolmogorov–Smirnov test) and equality of variance (Bartlett's test for equal variance). For multiple comparisons, Tukey's honesty post hoc test was employed and the corrected *$p < 0.05$, **$p < 0.01$, ***$p < 0.001$ are indicated, two-sided. Boxplots represent median and 25th/75th percentiles and their whiskers the data range. In some of the plots, outlier values are not shown for clarity of presentation, but all data points and animal were always included in the statistical analysis. The exact number of replications for each experiment is detailed in the text and figures.

## Supplementary Material

Refer to Web version on PubMed Central for supplementary material.

## ACKNOWLEDGMENTS

We thank Dr. Michael A. Long for valuable comments, Dr. Guoling Tian for technical support, and Tsien lab members for discussions. S.C. was supported by a senior biomedical postdoctoral fellowship from the Charles H. Revson Foundation, a postdoctoral fellowship from the Fonds de Recherche en Santé Qué bec, and a K99/R00 Pathway to Independence Award from NIMH (1K99MH126157-01). M.V. was supported by postdoctoral fellowships from the European Molecular Biology Organization (EMBO ALTF 1161-2017) and Human Frontiers Science Program (LT0000717/2018). R.E. was supported by a Research Fellowship from the Deutsche Forschungsgemeinschaft (EG 401/1-1). S.B.L. was supported by postdoctoral fellowships from the NIA (1T32AG052909-01A1) and the Alzheimer's Association (AARF-21-852397). G.B.'s lab was supported by NIH MH107396, NS 090583, NSF PIRE (grant no. 1545858), and U19 NS107616. R.W.T. received grants from the NINDS (1U19NS107616-02), NIDA (R01 DA040484-04), and NIMH (R01 MH071739-15).

## REFERENCES

1. Klausberger T, and Somogyi P (2008). Neuronal diversity and temporal dynamics: the unity of hippocampal circuit operations. Science 321, 53–57. 10.1126/science.1149381. [PubMed: 18599766]
2. Pelkey KA, Chittajallu R, Craig MT, Tricoire L, Wester JC, and McBain CJ (2017). Hippocampal GABAergic inhibitory interneurons. Physiol. Rev. 97, 1619–1747.10.1152/physrev.00007.2017. [PubMed: 28954853]
3. Freund TF, and Buzsáki G (1996). Interneurons of the hippocampus. Hippocampus 6, 347–470. 10.1002/(SICI)1098-1063(1996)6:4<347::AID-HIPO1>3.0.CO;2-I. [PubMed: 8915675]
4. Stark E, Eichler R, Roux L, Fujisawa S, Rotstein HG, and Buzsáki G (2013). Inhibition-induced theta resonance in cortical circuits. Neuron 80, 1263–1276. 10.1016/j.neuron.2013.09.033. [PubMed: 24314731]
5. Cardin JA, Carlé n M, Meletis K, Knoblich U, Zhang F, Deisseroth K, Tsai LH, and Moore CI (2009). Driving fast-spiking cells induces gamma rhythm and controls sensory responses. Nature 459, 663–667. 10.1038/nature08002. [PubMed: 19396156]
6. Sohal VS, Zhang F, Yizhar O, and Deisseroth K (2009). Parvalbumin neurons and gamma rhythms enhance cortical circuit performance. Nature 459, 698–702. 10.1038/nature07991. [PubMed: 19396159]
7. McKenna JT, Thankachan S, Uygun DS, Shukla C, McNally JM, Schiffino FL, Cordeira J, Katsuki F, Zant JC, Gamble MC, et al. (2020). Basal forebrain parvalbumin neurons mediate arousals from sleep induced by hypercarbia or auditory stimuli. Curr. Biol. 30, 2379–2385.e4. 10.1016/j.cub.2020.04.029. [PubMed: 32413301]
8. Donato F, Rompani SB, and Caroni P (2013). Parvalbumin-expressing basket-cell network plasticity induced by experience regulates adult learning. Nature 504, 272–276. 10.1038/nature12866. [PubMed: 24336286]
9. Kuhlman SJ, Olivas ND, Tring E, Ikrar T, Xu X, and Trachtenberg JT (2013). A disinhibitory microcircuit initiates critical-period plasticity in the visual cortex. Nature 501, 543–546. 10.1038/nature12485. [PubMed: 23975100]
10. Amilhon B, Huh CY, Manseau F, Ducharme G, Nichol H, Adamantidis A, and Williams S (2015). Parvalbumin interneurons of hippocampus tune population activity at theta frequency. Neuron 86, 1277–1289. 10.1016/j.neuron.2015.05.027. [PubMed: 26050044]
11. Royer S, Zemelman BV, Losonczy A, Kim J, Chance F, Magee JC, and Buzsáki G (2012). Control of timing, rate and bursts of hippocampal place cells by dendritic and somatic inhibition. Nat. Neurosci. 15, 769–775. 10.1038/nn.3077. [PubMed: 22446878]
12. Sik A, Penttonen M, Ylinen A, and Buzsáki G (1995). Hippocampal CA1 interneurons: an in vivo intracellular labeling study. J. Neurosci. 15, 6651–6665. [PubMed: 7472426]

13. Bartos M, Vida I, Frotscher M, Meyer A, Monyer H, Geiger JR, and Jonas P (2002). Fast synaptic inhibition promotes synchronized gamma oscillations in hippocampal interneuron networks. Proc. Natl. Acad. Sci. USA 99, 13222–13227. 10.1073/pnas.192233099. [PubMed: 12235359]
14. Kawaguchi Y, Katsumaru H, Kosaka T, Heizmann CW, and Hama K (1987). Fast spiking cells in rat hippocampus (CA1 region) contain the calcium-binding protein parvalbumin. Brain Res. 416, 369–374. 10.1016/0006-8993(87)90921-8. [PubMed: 3304536]
15. Rudy B, and McBain CJ (2001). Kv3 channels: voltage-gated K+ channels designed for high-frequency repetitive firing. Trends Neurosci. 24, 517–526. 10.1016/s0166-2236(00)01892-0. [PubMed: 11506885]
16. Klausberger T, Magill PJ, Márton LF, Roberts JD, Cobden PM, Buzsáki G, and Somogyi P (2003). Brain-state- and cell-type-specific firing of hippocampal interneurons in vivo. Nature 421, 844–848. 10.1038/nature01374. [PubMed: 12594513]
17. Klausberger T, Márton LF, Baude A, Roberts JD, Magill PJ, and Somogyi P (2004). Spike timing of dendrite-targeting bistratified cells during hippocampal network oscillations in vivo. Nat. Neurosci. 7, 41–47. 10.1038/nn1159. [PubMed: 14634650]
18. Cobb SR, Buhl EH, Halasy K, Paulsen O, and Somogyi P (1995). Synchronization of neuronal activity in hippocampus by individual GABAergic interneurons. Nature 378, 75–78. 10.1038/378075a0. [PubMed: 7477292]
19. Chamberland S, and Topolnik L (2012). Inhibitory control of hippocampal inhibitory neurons. Front. Neurosci. 6, 165. 10.3389/fnins.2012.00165. [PubMed: 23162426]
20. Letzkus JJ, Wolff SB, Meyer EM, Tovote P, Courtin J, Herry C, and Lüthi A (2011). A disinhibitory microcircuit for associative fear learning in the auditory cortex. Nature 480, 331–335. 10.1038/nature10674. [PubMed: 22158104]
21. Wolff SB, Gründemann J, Tovote P, Krabbe S, Jacobson GA, Müller C, Herry C, Ehrlich I, Friedrich RW, Letzkus JJ, et al. (2014). Amygdala interneuron subtypes control fear learning through disinhibition. Nature 509, 453–458. 10.1038/nature13258. [PubMed: 24814341]
22. Buzsáki G, Leung LW, and Vanderwolf CH (1983). Cellular bases of hippocampal EEG in the behaving rat. Brain Res. 287, 139–171. 10.1016/0165-0173(83)90037-1. [PubMed: 6357356]
23. Lytton WW, and Sejnowski TJ (1991). Simulations of cortical pyramidal neurons synchronized by inhibitory interneurons. J. Neurophysiol. 66, 1059–1079. 10.1152/jn.1991.66.3.1059. [PubMed: 1661324]
24. Wang XJ, and Buzsáki G (1996). Gamma oscillation by synaptic inhibition in a hippocampal interneuronal network model. J. Neurosci. 16, 6402–6413. [PubMed: 8815919]
25. Bartos M, Vida I, and Jonas P (2007). Synaptic mechanisms of synchronized gamma oscillations in inhibitory interneuron networks. Nat. Rev. Neurosci. 8, 45–56. 10.1038/nrn2044. [PubMed: 17180162]
26. Lovett-Barron M, Turi GF, Kaifosh P, Lee PH, Bolze F, Sun XH, Nicoud JF, Zemelman BV, Sternson SM, and Losonczy A (2012). Regulation of neuronal input transformations by tunable dendritic inhibition. Nat. Neurosci. 15, 423–430. 10.1038/nn.3024. [PubMed: 22246433]
27. Acsády L, Görcs TJ, and Freund TF (1996). Different populations of vasoactive intestinal polypeptide-immunoreactive interneurons are specialized to control pyramidal cells or interneurons in the hippocampus. Neuroscience 73, 317–334. 10.1016/0306-4522(95)00609-5. [PubMed: 8783252]
28. Gulyás AI, Megías M, Emri Z, and Freund TF (1999). Total number and ratio of excitatory and inhibitory synapses converging onto single interneurons of different types in the CA1 area of the rat hippocampus. J. Neurosci. 19, 10082–10097. [PubMed: 10559416]
29. Bartos M, Vida I, Frotscher M, Geiger JR, and Jonas P (2001). Rapid signaling at inhibitory synapses in a dentate gyrus interneuron network. J. Neurosci. 21, 2687–2698. [PubMed: 11306622]
30. Tricoire L, Pelkey KA, Erkkila BE, Jeffries BW, Yuan X, and McBain CJ (2011). A blueprint for the spatiotemporal origins of mouse hippocampal interneuron diversity. J. Neurosci. 31, 10948–10970. 10.1523/JNEUROSCI.0323-11.2011. [PubMed: 21795545]

31. Gentet LJ, Avermann M, Matyas F, Staiger JF, and Petersen CC (2010). Membrane potential dynamics of GABAergic neurons in the barrel cortex of behaving mice. Neuron 65, 422–435. 10.1016/j.neuron.2010.01.006. [PubMed: 20159454]
32. Yu J, Gutnisky DA, Hires SA, and Svoboda K (2016). Layer 4 fast-spiking interneurons filter thalamocortical signals during active somatosensation. Nat. Neurosci. 19, 1647–1657. 10.1038/nn.4412. [PubMed: 27749825]
33. Egorov AV, Hamam BN, Fransén E, Hasselmo ME, and Alonso AA (2002). Graded persistent activity in entorhinal cortex neurons. Nature 420, 173–178. 10.1038/nature01171. [PubMed: 12432392]
34. Fransén E, Tahvildari B, Egorov AV, Hasselmo ME, and Alonso AA (2006). Mechanism of graded persistent cellular activity of entorhinal cortex layer v neurons. Neuron 49, 735–746. 10.1016/j.neuron.2006.01.036. [PubMed: 16504948]
35. Sheffield ME, Best TK, Mensh BD, Kath WL, and Spruston N (2011). Slow integration leads to persistent action potential firing in distal axons of coupled interneurons. Nat. Neurosci. 14, 200–207. 10.1038/nn.2728. [PubMed: 21150916]
36. Shu Y, Hasenstaub A, and McCormick DA (2003). Turning on and off recurrent balanced cortical activity. Nature 423, 288–293. 10.1038/nature01616. [PubMed: 12748642]
37. Cui ED, and Strowbridge BW (2019). Selective attenuation of ether-ago-go related K(+) currents by endogenous acetylcholine reduces spike-frequency adaptation and network correlation. eLife 8, e44954. 10.7554/eLife.44954. [PubMed: 31032798]
38. Kiehn O, and Eken T (1998). Functional role of plateau potentials in vertebrate motor neurons. Curr. Opin. Neurobiol. 8, 746–752. 10.1016/s0959-4388(98)80117-7. [PubMed: 9914232]
39. Jinno S, and Kosaka T (2000). Colocalization of parvalbumin and somatostatin-like immunoreactivity in the mouse hippocampus: quantitative analysis with optical dissector. J. Comp. Neurol. 428, 377–388. [PubMed: 11074441]
40. Harris KD, Hochgerner H, Skene NG, Magno L, Katona L, Bengtsson Gonzales C, Somogyi P, Kessaris N, Linnarsson S, and Hjerling-Leffler J (2018). Classes and continua of hippocampal CA1 inhibitory neurons revealed by single-cell transcriptomics. PLOS Biol. 16, e2006387. 10.1371/journal.pbio.2006387. [PubMed: 29912866]
41. Udakis M, Pedrosa V, Chamberlain SEL, Clopath C, and Mellor JR (2020). Interneuron-specific plasticity at parvalbumin and somatostatin inhibitory synapses onto CA1 pyramidal neurons shapes hippocampal output. Nat. Commun. 11, 4395. 10.1038/s41467-020-18074-8. [PubMed: 32879322]
42. Vida I, Bartos M, and Jonas P (2006). Shunting inhibition improves robustness of gamma oscillations in hippocampal interneuron networks by homogenizing firing rates. Neuron 49, 107–117. 10.1016/j.neuron.2005.11.036. [PubMed: 16387643]
43. Otsu Y, Donneger F, Schwartz EJ, and Poncer JC (2020). Cation-chloride cotransporters and the polarity of GABA signalling in mouse hippocampal parvalbumin interneurons. J. Physiol. 598, 1865–1880. 10.1113/JP279221. [PubMed: 32012273]
44. Bartos M, and Elgueta C (2012). Functional characteristics of parvalbumin- and cholecystokinin-expressing basket cells. J. Physiol. 590, 669–681. 10.1113/jphysiol.2011.226175. [PubMed: 22250212]
45. Valero M, Viney TJ, Machold R, Mederos S, Zutshi I, Schuman B,Senzai Y, Rudy B, and Buzsáki G (2021). Sleep down state-active ID2/Nkx2.1 interneurons in the neocortex. Nat. Neurosci. 24, 401–411. 10.1038/s41593-021-00797-6. [PubMed: 33619404]
46. Henze DA, Borhegyi Z, Csicsvari J, Mamiya A, Harris KD, and Buzsáki G (2000). Intracellular features predicted by extracellular recordings in the hippocampus in vivo. J. Neurophysiol. 84, 390–400. 10.1152/jn.2000.84.1.390. [PubMed: 10899213]
47. Eyring KW, Liu J, König GM, Hidema S, Nishimori K, Kostenis E, and Tsien RW (2020). Oxytocin signals via Gi and Gq to drive persistent CA2 pyramidal cell firing and strengthen CA3-CA1 neurotransmission. 10.1101/2020.05.07.082727.
48. Chamberland S, Salesse C, Topolnik D, and Topolnik L (2010). Synapse-specific inhibitory control of hippocampal feedback inhibitory circuit. Front. Cell. Neurosci. 4, 130. 10.3389/fncel.2010.00130. [PubMed: 21060720]

49. Tyan L, Chamberland S, Magnin E, Camiré O, Francavilla R, David LS, Deisseroth K, and Topolnik L (2014). Dendritic inhibition provided by interneuron-specific cells controls the firing rate and timing of the hippocampal feedback inhibitory circuitry. J. Neurosci. 34, 4534–4547. 10.1523/JNEUROSCI.3813-13.2014. [PubMed: 24671999]
50. Francavilla R, Villette V, Luo X, Chamberland S, Muñoz-Pino E, Camiré O, Wagner K, Kis V, Somogyi P, and Topolnik L (2018). Connectivity and network state-dependent recruitment of long-range VIP-GABAergic neurons in the mouse hippocampus. Nat. Commun. 9, 5043. 10.1038/s41467-018-07162-5. [PubMed: 30487571]
51. Turi GF, Li WK, Chavlis S, Pandi I, O'Hare J, Priestley JB, Grosmark AD, Liao Z, Ladow M, Zhang JF, et al. (2019). Vasoactive intestinal polypeptide-expressing interneurons in the hippocampus support goal-oriented spatial learning. Neuron 101, 1150–1165.e8. 10.1016/j.neuron.2019.01.009. [PubMed: 30713030]
52. Cembrowski MS, Wang L, Sugino K, Shields BC, and Spruston N (2016). Hipposeq: a comprehensive RNA-seq database of gene expression in hippocampal principal neurons. eLife 5, e14997. 10.7554/eLife.14997. [PubMed: 27113915]
53. Goldberg EM, Clark BD, Zagha E, Nahmani M, Erisir A, and Rudy B (2008). K+ channels at the axon initial segment dampen near-threshold excitability of neocortical fast-spiking GABAergic interneurons. Neuron 58, 387–400. 10.1016/j.neuron.2008.03.003. [PubMed: 18466749]
54. Connor JA, and Stevens CF (1971). Prediction of repetitive firing behaviour from voltage clamp data on an isolated neurone soma. J. Physiol. 213, 31–53. 10.1113/jphysiol.1971.sp009366. [PubMed: 5575343]
55. Turrigiano GG, Marder E, and Abbott LF (1996). Cellular short-term memory from a slow potassium conductance. J. Neurophysiol. 75, 963–966. 10.1152/jn.1996.75.2.963. [PubMed: 8714669]
56. Khaliq ZM, and Bean BP (2008). Dynamic, nonlinear feedback regulation of slow pacemaking by A-type potassium current in ventral tegmental area neurons. J. Neurosci. 28, 10905–10917. 10.1523/JNEUROSCI.2237-08.2008. [PubMed: 18945898]
57. Campanac E, Gasselin C, Baude A, Rama S, Ankri N, and Debanne D (2013). Enhanced intrinsic excitability in basket cells maintains excitatory-inhibitory balance in hippocampal circuits. Neuron 77, 712–722. 10.1016/j.neuron.2012.12.020. [PubMed: 23439123]
58. Fricker D, and Miles R (2000). EPSP amplification and the precision of spike timing in hippocampal neurons. Neuron 28, 559–569. 10.1016/s0896-6273(00)00133-1. [PubMed: 11144364]
59. Miles R (1990). Synaptic excitation of inhibitory cells by single CA3 hippocampal pyramidal cells of the guinea-pig in vitro. J. Physiol. 428, 61–77. 10.1113/jphysiol.1990.sp018200. [PubMed: 2231426]
60. Golomb D, Donner K, Shacham L, Shlosberg D, Amitai Y, and Hansel D (2007). Mechanisms of firing patterns in fast-spiking cortical interneurons. PLoS Comput. Biol. 3, e156. 10.1371/journal.pcbi.0030156. [PubMed: 17696606]
61. Lien CC, Martina M, Schultz JH, Ehmke H, and Jonas P (2002). Gating, modulation and subunit composition of voltage-gated K(+) channels in dendritic inhibitory interneurones of rat hippocampus. J. Physiol. 538, 405–419. 10.1113/jphysiol.2001.013066. [PubMed: 11790809]
62. Owen SF, Tuncdemir SN, Bader PL, Tirko NN, Fishell G, and Tsien RW (2013). Oxytocin enhances hippocampal spike transmission by modulating fast-spiking interneurons. Nature 500, 458–462. 10.1038/nature12330. [PubMed: 23913275]
63. Tirko NN, Eyring KW, Carcea I, Mitre M, Chao MV, Froemke RC, and Tsien RW (2018). Oxytocin transforms firing mode of CA2 hippocampal neurons. Neuron 100, 593–608.e3. 10.1016/j.neuron.2018.09.008. [PubMed: 30293821]
64. Hirase H, Czurkó A, Csicsvari J, and Buzsáki G (1999). Firing rate and theta-phase coding by hippocampal pyramidal neurons during 'space clamping'. Eur. J. Neurosci. 11, 4373–4380. 10.1046/j.1460-9568.1999.00853.x. [PubMed: 10594664]
65. Wiener SI, Paul CA, and Eichenbaum H (1989). Spatial and behavioral correlates of hippocampal neuronal activity. J. Neurosci. 9, 2737–2763. [PubMed: 2769364]

66. Czurkó A, Hirase H, Csicsvari J, and Buzsáki G (1999). Sustained activation of hippocampal pyramidal cells by 'space clamping' in a running wheel. Eur. J. Neurosci. 11, 344–352. 10.1046/j.1460-9568.1999.00446.x. [PubMed: 9987037]

67. Hefft S, and Jonas P (2005). Asynchronous GABA release generates long-lasting inhibition at a hippocampal interneuron-principal neuron synapse. Nat. Neurosci. 8, 1319–1328. 10.1038/nn1542. [PubMed: 16158066]

68. Martina M, Schultz JH, Ehmke H, Monyer H, and Jonas P (1998). Functional and molecular differences between voltage-gated K+ channels of fast-spiking interneurons and pyramidal neurons of rat hippocampus. J. Neurosci. 18, 8111–8125. [PubMed: 9763458]

69. Hu H, and Jonas P (2014). A supercritical density of Na(+) channels ensures fast signaling in GABAergic interneuron axons. Nat. Neurosci. 17, 686–693. 10.1038/nn.3678. [PubMed: 24657965]

70. Lorincz A, and Nusser Z (2008). Cell-type-dependent molecular composition of the axon initial segment. J. Neurosci. 28, 14329–14340. 10.1523/JNEUROSCI.4833-08.2008. [PubMed: 19118165]

71. Prüss H, Grosse G, Brunk I, Veh RW, and Ahnert-Hilger G (2010). Age-dependent axonal expression of potassium channel proteins during development in mouse hippocampus. Histochem. Cell Biol. 133, 301–312. 10.1007/s00418-009-0668-z. [PubMed: 20012645]

72. Cohen SM, Suutari B, He X, Wang Y, Sanchez S, Tirko NN, Mandelberg NJ, Mullins C, Zhou G, Wang S, et al. (2018). Calmodulin shuttling mediates cytonuclear signaling to trigger experience-dependent transcription and memory. Nat. Commun. 9, 2451. 10.1038/s41467-018-04705-8. [PubMed: 29934532]

73. Hu H, Roth FC, Vandael D, and Jonas P (2018). Complementary tuning of Na(+) and K(+) channel gating underlies fast and energy-efficient action potentials in GABAergic interneuron axons. Neuron 98, 156–165.e6. 10.1016/j.neuron.2018.02.024. [PubMed: 29621485]

74. Kraushaar U, and Jonas P (2000). Efficacy and stability of quantal GABA release at a hippocampal interneuron-principal neuron synapse. J. Neurosci. 20, 5594–5607. [PubMed: 10908596]

75. Park C, Chen X, Tian CL, Park GN, Chenouard N, Lee H, Yeo XY, Jung S, Tsien RW, Bi GQ, and Park H (2021). Unique dynamics and exocytosis properties of GABAergic synaptic vesicles revealed by three-dimensional single vesicle tracking. Proc. Natl. Acad. Sci. USA 118. e2022133118. 10.1073/pnas.2022133118. [PubMed: 33622785]

76. Geiller T, Sadeh S, Rolotti SV, Blockus H, Vancura B, Negrean A, Murray AJ, Rózsa B, Polleux F, Clopath C, and Losonczy A (2022). Local circuit amplification of spatial selectivity in the hippocampus. Nature 601, 105–109. 10.1038/s41586-021-04169-9. [PubMed: 34853473]

77. Pouille F, and Scanziani M (2001). Enforcement of temporal fidelity in pyramidal cells by somatic feed-forward inhibition. Science 293, 1159–1163. 10.1126/science.1060342. [PubMed: 11498596]

78. Buzsáki G, and Eidelberg E (1982). Direct afferent excitation and long-term potentiation of hippocampal interneurons. J. Neurophysiol. 48, 597–607. 10.1152/jn.1982.48.3.597. [PubMed: 6290613]

79. Mizuseki K, Sirota A, Pastalkova E, and Buzsáki G (2009). Theta oscillations provide temporal windows for local circuit computation in the entorhinal-hippocampal loop. Neuron 64, 267–280. 10.1016/j.neuron.2009.08.037. [PubMed: 19874793]

80. Mizuseki K, Royer S, Diba K, and Buzsáki G (2012). Activity dynamics and behavioral correlates of CA3 and CA1 hippocampal pyramidal neurons. Hippocampus 22, 1659–1680. 10.1002/hipo.22002. [PubMed: 22367959]

81. Schlingloff D, Káli S, Freund TF, Hájos N, and Gulyás AI (2014). Mechanisms of sharp wave initiation and ripple generation. J. Neurosci. 34, 11385–11398. 10.1523/JNEUROSCI.0867-14.2014. [PubMed: 25143618]

82. Viney TJ, Lasztoczi B, Katona L, Crump MG, Tukker JJ, Klausberger T, and Somogyi P (2013). Network state-dependent inhibition of identified hippocampal CA3 axo-axonic cells in vivo. Nat. Neurosci. 16, 1802–1811. 10.1038/nn.3550. [PubMed: 24141313]

83. Ylinen A, Bragin A, Nádasdy Z, Jandó G, Szabó I, Sik A, and Buzsáki G (1995). Sharp wave-associated high-frequency oscillation (200 Hz) in the intact hippocampus: network and intracellular mechanisms. J. Neurosci. 15, 30–46. [PubMed: 7823136]

84. Csicsvari J, Hirase H, Czurkó A, Mamiya A, and Buzsáki G (1999). Oscillatory coupling of hippocampal pyramidal cells and interneurons in the behaving Rat. J. Neurosci. 19, 274–287. [PubMed: 9870957]

85. Evangelista R, Cano G, Cooper C, Schmitz D, Maier N, and Kempter R (2020). Generation of sharp wave-ripple events by disinhibition. J. Neurosci. 40, 7811–7836. 10.1523/JNEUROSCI.2174-19.2020. [PubMed: 32913107]

86. Fernández-Ruiz A, Oliva A, Fermino de Oliveira E, Rocha-Almeida F, Tingley D, and Buzsáki G (2019). Long-duration hippocampal sharp wave ripples improve memory. Science 364, 1082–1086. 10.1126/science.aax0758. [PubMed: 31197012]

87. Muñoz W, Tremblay R, Levenstein D, and Rudy B (2017). Layer-specific modulation of neocortical dendritic inhibition during active wakefulness. Science 355, 954–959. 10.1126/science.aag2599. [PubMed: 28254942]

88. Lee S, Kruglikov I, Huang ZJ, Fishell G, and Rudy B (2013). A disinhibitory circuit mediates motor integration in the somatosensory cortex. Nat. Neurosci. 16, 1662–1670. 10.1038/nn.3544. [PubMed: 24097044]

89. Karnani MM, Jackson J, Ayzenshtat I, Hamzehei Sichani A, Manoocheri K, Kim S, and Yuste R (2016). Opening holes in the blanket of inhibition: localized lateral disinhibition by VIP interneurons. J. Neurosci. 36, 3471–3480. 10.1523/JNEUROSCI.3646-15.2016. [PubMed: 27013676]

90. Durstewitz D, Seamans JK, and Sejnowski TJ (2000). Neurocomputational models of working memory. Nat. Neurosci. 3, 1184–1191. 10.1038/81460. [PubMed: 11127836]

91. Shu Y, Hasenstaub A, Badoual M, Bal T, and McCormick DA (2003). Barrages of synaptic activity control the gain and sensitivity of cortical neurons. J. Neurosci. 23, 10388–10401. [PubMed: 14614098]

92. Tahvildari B, Fransén E, Alonso AA, and Hasselmo ME (2007). Switching between "On" and "Off" states of persistent activity in lateral entorhinal layer III neurons. Hippocampus 17, 257–263. 10.1002/hipo.20270. [PubMed: 17315198]

93. Loewenstein Y, Mahon S, Chadderton P, Kitamura K, Sompolinsky H, Yarom Y, and Häusser M (2005). Bistability of cerebellar Purkinje cells modulated by sensory stimulation. Nat. Neurosci. 8, 202–211. 10.1038/nn1393. [PubMed: 15665875]

94. Heyward P, Ennis M, Keller A, and Shipley MT (2001). Membrane bistability in olfactory bulb mitral cells. J. Neurosci. 21, 5311–5320. [PubMed: 11438607]

95. Fuentealba P, Timofeev I, Bazhenov M, Sejnowski TJ, and Steriade M (2005). Membrane bistability in thalamic reticular neurons during spindle oscillations. J. Neurophysiol. 93, 294–304. 10.1152/jn.00552.2004. [PubMed: 15331618]

96. Deemyad T, Lüthi J, and Spruston N (2018). Astrocytes integrate and drive action potential firing in inhibitory subnetworks. Nat. Commun. 9, 4336. 10.1038/s41467-018-06338-3. [PubMed: 30337521]

97. Shen B, Louie K, and Glimcher P (2022). Flexible control of representational dynamics in a disinhibition-based model of decision making. 10.1101/2022.04.18.488670.

98. Marlin BJ, Mitre M, D'amour JA, Chao MV, and Froemke RC (2015). Oxytocin enables maternal behaviour by balancing cortical inhibition. Nature 520, 499–504. 10.1038/nature14402. [PubMed: 25874674]

99. Magee JC, and Grienberger C (2020). Synaptic plasticity forms and functions. Annu. Rev. Neurosci. 43, 95–117. 10.1146/annurev-neuro-090919-022842. [PubMed: 32075520]

100. Petersen PC, Siegle JH, Steinmetz NA, Mahallati S, and Buzsáki G (2021). CellExplorer: A framework for visualizing and characterizing single neurons. Neuron 109, 3594–3608.e2. 10.1016/j.neuron.2021.09.002. [PubMed: 34592168]

101. Hu H, Cavendish JZ, and Agmon A (2013). Not all that glitters is gold: off-target recombination in the somatostatin-IRES-Cre mouse line labels a subset of fast-spiking interneurons. Front. Neural Circuits 7, 195. 10.3389/fncir.2013.00195. [PubMed: 24339803]

102. Anastasiades PG, Marlin JJ, and Carter AG (2018). Cell-type specificity of callosally evoked excitation and feedforward inhibition in the prefrontal cortex. Cell Rep. 22, 679–692. 10.1016/j.celrep.2017.12.073. [PubMed: 29346766]

103. Valero M, Zutshi I, Yoon E, and Buzsáki G (2022). Probing subthreshold dynamics of hippocampal neurons by pulsed optogenetics. Science 375, 570–574. 10.1126/science.abm1891. [PubMed: 35113721]

## Highlights

- Synaptic inhibition of fast-spiking interneurons persistently interrupts their firing
- The interruption of firing is driven by GABAergic conductance but far outlasts it
- Near-balancing Na and K conductances sustain a quiescent yet hyperexcitable state
- The persistent interruption of firing disinhibits CA1 pyramidal cells

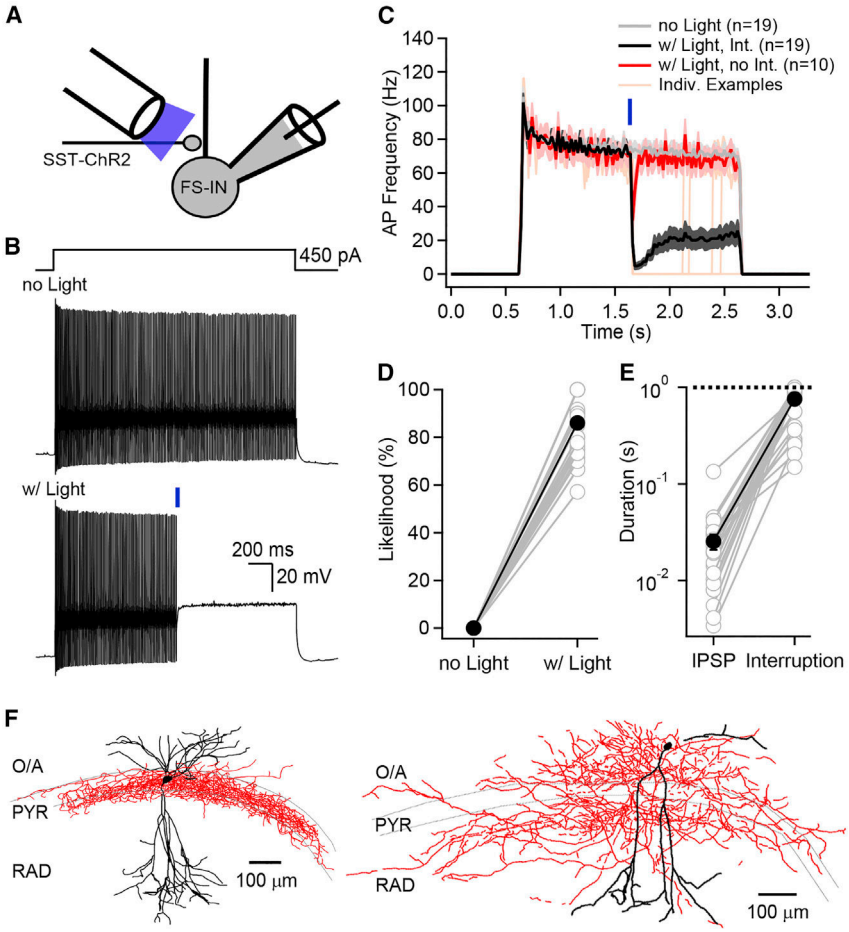


**Figure 1. Synaptic inhibition persistently interrupts firing of PV-Ins**

(A) Recording configuration.

(B) PV-INs depolarized with rectangular current waveform. Optogenetic stimulation (blue bar) generated an IPSP followed by a persistent interruption of firing.

(C) Summary data, firing frequency vs. time for experiments exemplified in (B), with optogenetic stimulation (black) or without (light gray). Red trace, average of traces with light but when no interruption was induced; orange traces, exemplar trials.

(D) Likelihood of observing an interruption. Collective results from PV-INs shown in (C) and 10 additional neurons.

(E) Duration of IPSP compared with silent period associated with interruption. The dashed line represents the 1-s duration of the depolarizing step, a cap on the interruption duration.

(F) Neurolucida reconstructions of recorded PV-INs. Dendrites black, axon red.

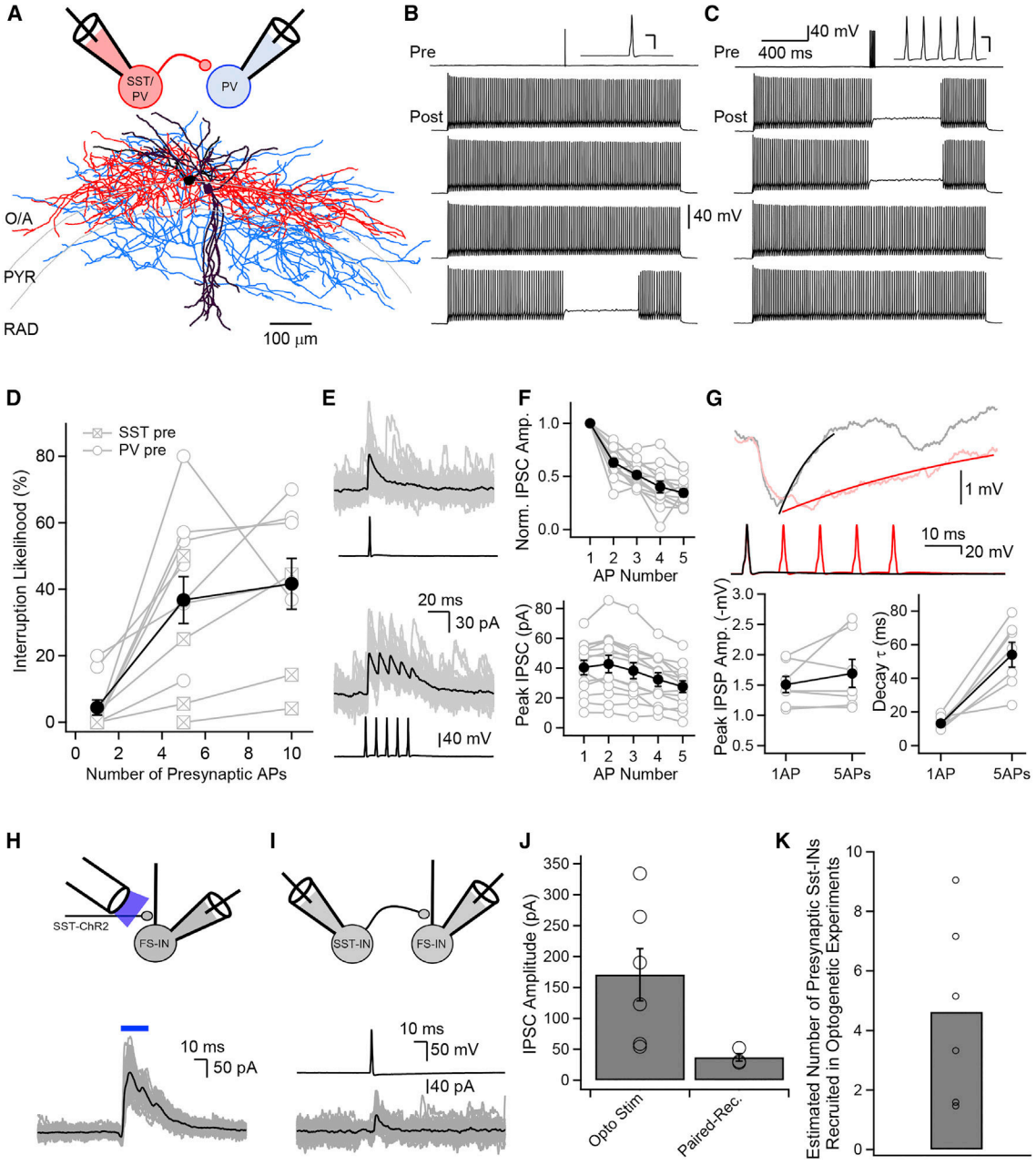


**Figure 2. A single presynaptic interneuron can interrupt PV-IN firing**

(A) Recording configuration and Neurolucida reconstruction of a synaptically connected pair of INs. Dendrites of presynaptic IN shown in black, axon in red. Dendrites of postsynaptic neurons shown in purple, axon in blue.

(B) Current-clamp recordings in a pair of INs. A single AP in the presynaptic cell suffices to interrupt postsynaptic firing occasionally. Four consecutive epochs shown.

(C) Same pair as in (B), with five APs at 100 Hz. Insets, AP for (B) and (C); calibration: 40 mV vertical, 5 ms horizontal.

(D) Interruption likelihood varies with number of presynaptic APs. Five- and ten-AP bursts delivered at 100 Hz. Depolarizing current pulse amplitude in postsynaptic PV-INs, 255 ± 23

pA (n = 11). Presynaptic PV- and SST-INs had similar likelihood to interrupt firing when five APs were evoked (n = 7 and n = 4, respectively; p = 0.11).

(E) IPSCs recorded at 0 mV in PV-INs. Black traces, average of 50 consecutive sweeps (gray).

(F) Top, normalized IPSC amplitude, measured from trough-to-peak, vs. stimulus number. Bottom, absolute peak amplitudes of the IPSC burst from prestimulus baseline.

(G) Top, current-clamp recordings of single- (black) and five-AP- (red) evoked IPSPs (averages of 3 consecutive sweeps). Bottom, with AP repetition, peak IPSP amplitude hardly changed, whereas decay time constant greatly increased.

(H–J) IPSCs measured in optogenetic experiments (H), in paired recordings (I); pooled data of IPSC amplitudes (J).

(K) Ratio of values in (J) provides estimate of number of optogenetically activated SST-INs synapsing onto a PV-IN.

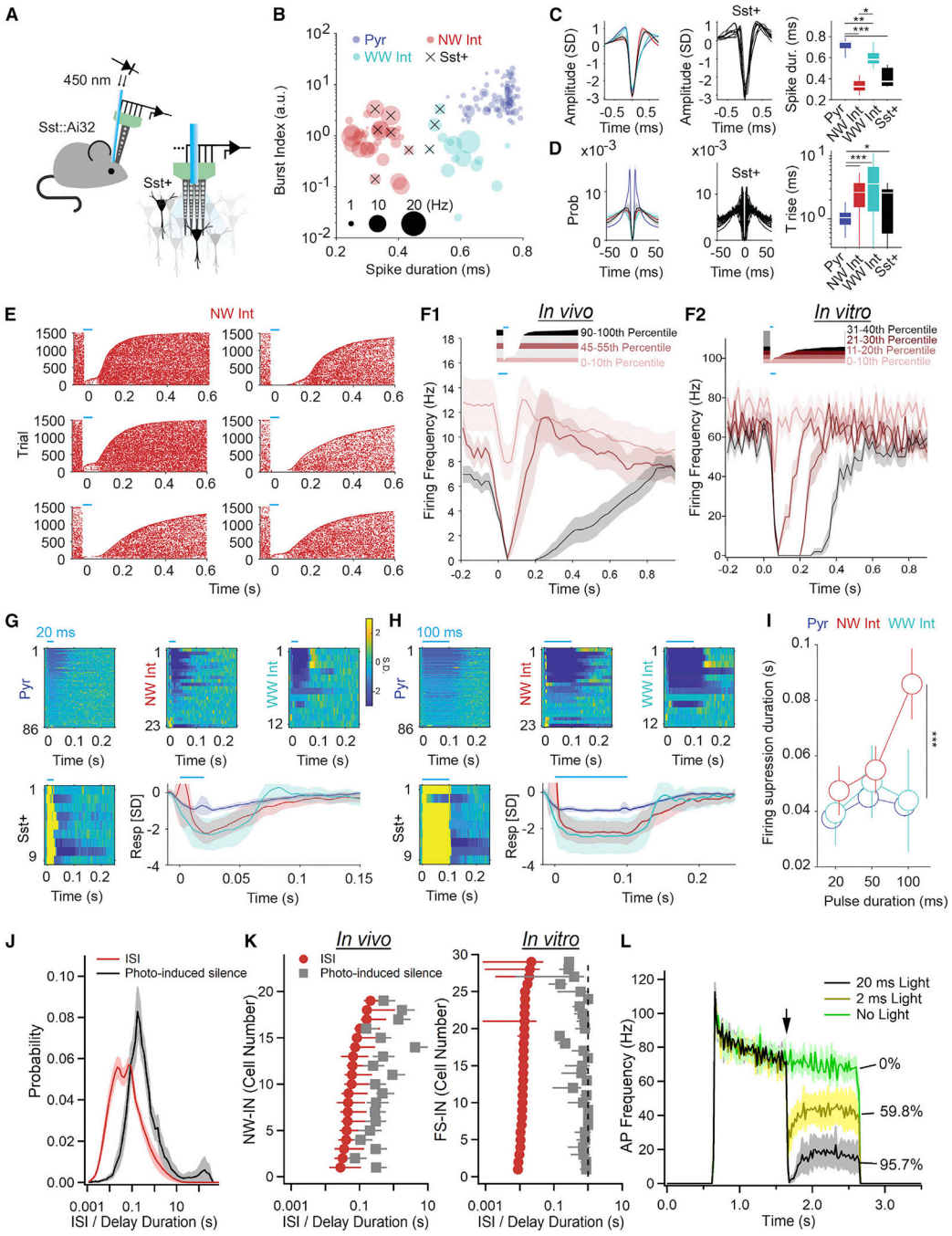


**Figure 3. PV-IN silencing persists following optogenetic stimulation *in vivo***

(A) Recording configuration of multisite silicon probe and optical fiber in CA1.

(B) Burst index as a function of spike duration for all neurons sampled (n = 130 units) distinguishes NW-INs (red), CA1-PYRs (blue), WW-INs (teal), and SST-INs (black ×).

(C) Average spike waveform for populations identified in (B) (left), including SST-INs (middle), and trough-to-peak spike duration (right).

(D) Same as in (C) for firing auto-correlograms and rise time to peak ($p < 0.001$ for PYR vs. NW-IN).

(E) AP raster plots of 6 representative NW-INs during 1,500 trials, ranked by silencing duration induced by 50 ms optogenetic stimulation (blue bars).
(F) (F1) Summary graph for all NW-INs sampled, showing the averages of trials across neurons for the lowest, middle, and highest deciles. (F2) Similar analysis performed on *in vitro* data qualitatively parallels the findings in (F1) (see discussion).
(G–I) Optogenetic stimulation for 20 ms (G) or 100 ms (H) in other cell types results in briefer silencing duration than in NW-INs. Warmer colors correspond to higher firing rates (inset). (I) Delay to recovery of spiking as a function of optogenetic stimulation duration.
(J) The distributions of inter-spike intervals (ISIs) and optogenetic-induced silence duration for NW-INs are significantly different (Kolmogorov-Smirnov test: $p < 0.0001$, $K = 0.7$).
(K) Average of ISIs and optogenetic-induced silences for individual neurons, *in vivo* and *in vitro*.
(L) Effect of varying optogenetic stimulus strength on the apparent interruption duration *in vitro*. *$p < 0.05$; **$p < 0.01$; ***$p < 0.001$ for all statistical tests.

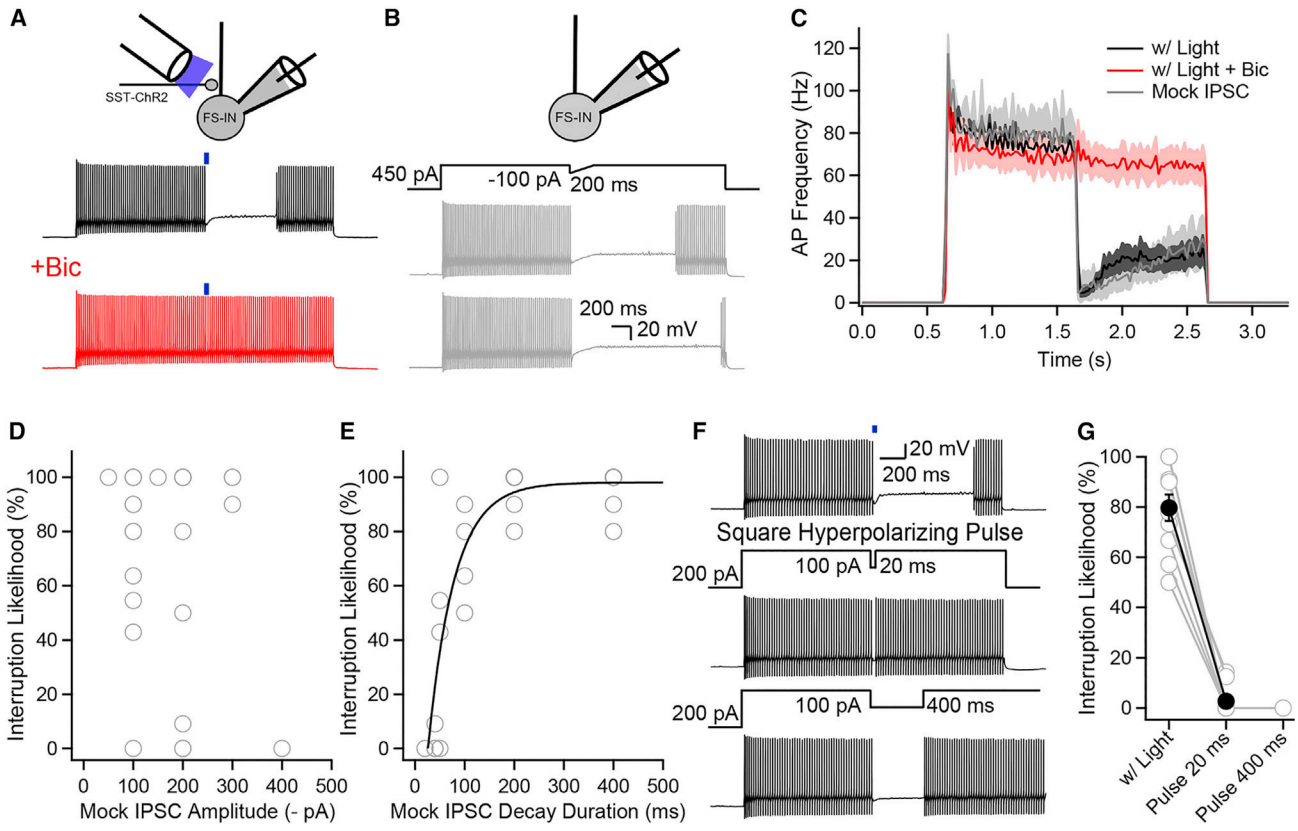


**Figure 4. Postsynaptic hyperpolarizations through $GABA_AR$ activation or current injection interrupt PV-Ins**

(A) Bicuculline (10 μM) abolishes optogenetically induced interruption of firing.

(B) Hyperpolarizing current injections (mock IPSCs) reliably interrupt PV-INs.

(C) AP frequency vs. time for optogenetically evoked stimulation before (black) and after Bic (red). Data also shown for mock-IPSC-induced interruption (gray).

(D) Interruption likelihood vs. mock-IPSC amplitude.

(E) Interruption likelihood vs. mock-IPSC duration. Exponential fit shown.

(F) Rectangular hyperpolarizing pulse (20 or 400 ms) fails to interrupt firing.

(G) Interruption likelihood for paired experiments with optogenetic stimulation or rectangular hyperpolarizing pulses.

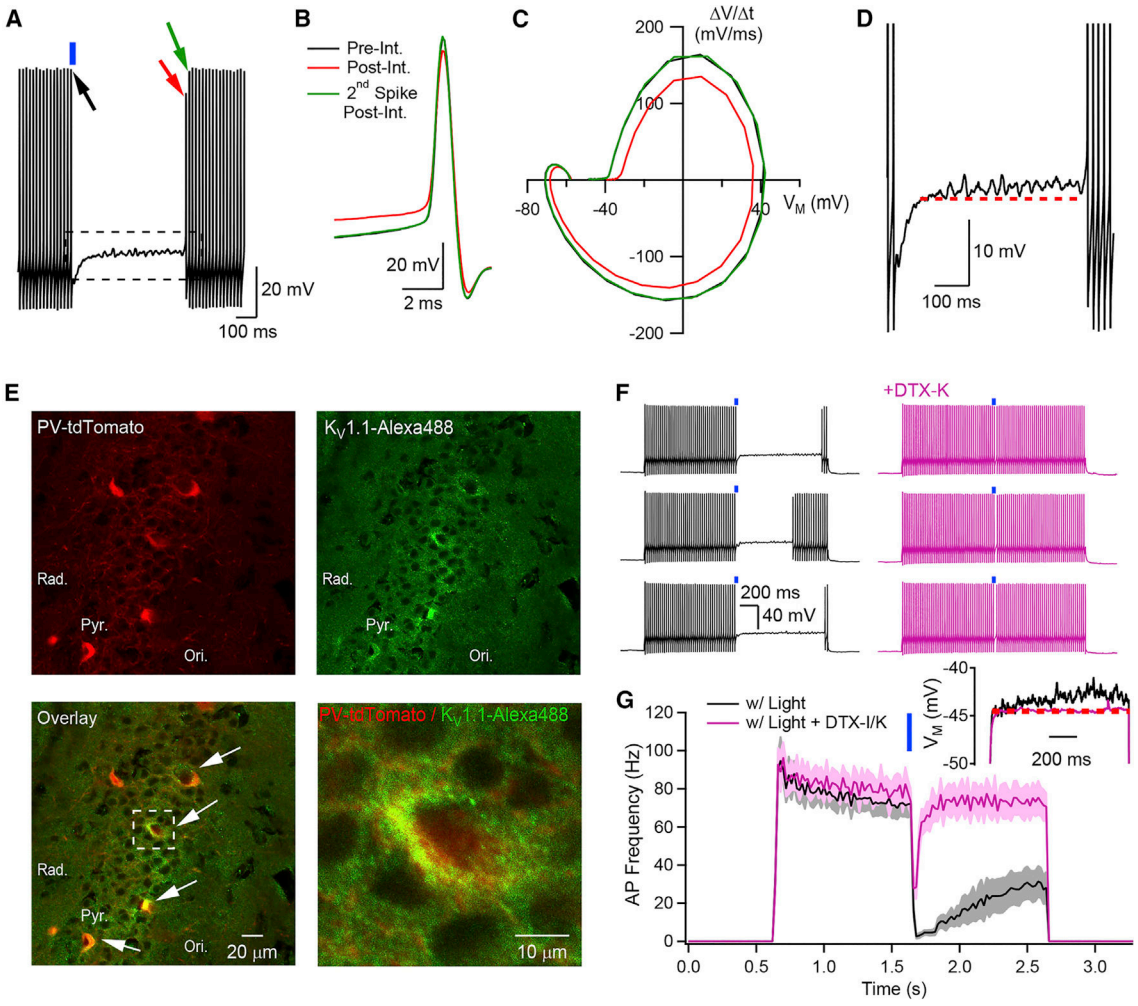


**Figure 5. $K_V1.1$ is required for interruption of firing**

(A) Current-clamp recording from a PV-IN.

(B) Zoomed-in data from (A), showing the three APs indicated by arrows.

(C) Phase-plane plot for the three APs in (B).

(D) During the interruption, the $V_M$ undergoes subthreshold oscillations and gradually depolarizes (dashed line, constant $V_M$ reference).

(E) Immunohistochemistry reveals that $K_v1.1$ is expressed in PV-INs in regions bordering CA1-PYR layer. White arrows, PV-INs with strong somatic $K_V1.1$ expression.

(F) Optogenetically induced interruption before (black) and after (purple) exposure to DTX-K (three consecutive epochs each).

(G) AP frequency vs. time for experiments in absence or presence of DTX-K or DTX-I. Inset: DTX-K prevents gradual membrane depolarization.

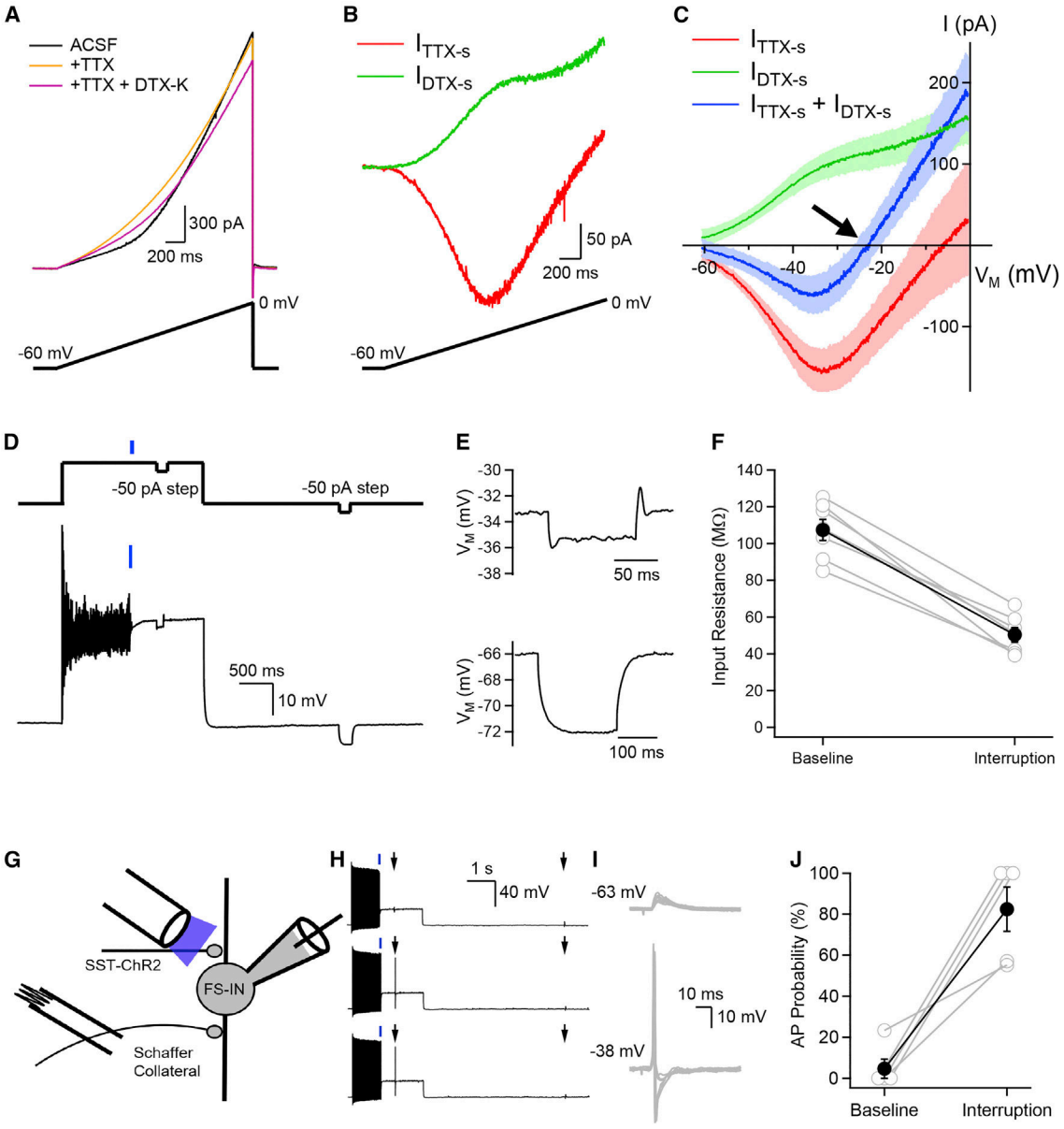


**Figure 6. Interplay between $K_V1.1$-current and $Na^+$-dependent current can support a stable point in $V_M$, a depolarized yet hyperresponsive state**

(A) Voltage-clamp recordings from a PV-IN in control (black), in TTX (gold) and with both TTX and DTX-K (purple).

(B) Arithmetic subtraction reveals $I_{DTX\text{-}s}$ and $I_{TTX\text{-}s}$.

(C) Current vs. voltage. $I_{DTX\text{-}s}$ and $I_{TTX\text{-}s}$ measured in same neurons; shaded areas, standard error.

(D) $V_M$ dynamics during the firing interruption.

(E) $V_M$ responses to hyperpolarizing current pulses, during interruption (top) or at resting $V_M$ (bottom).

(F) Input resistance measured at baseline and during interruption.

(G) Experimental design, including fixed amplitude stimulation.

(H) Three consecutive sweeps, subthreshold EPSPs at rest become suprathreshold during the interruption.
(I) Changes in $V_M$ evoked by Schaffer collateral stimulation at resting potential (top) or during the interruption (bottom).
(J) AP probability for stimuli delivered at resting $V_M$ (baseline) or during interruption.

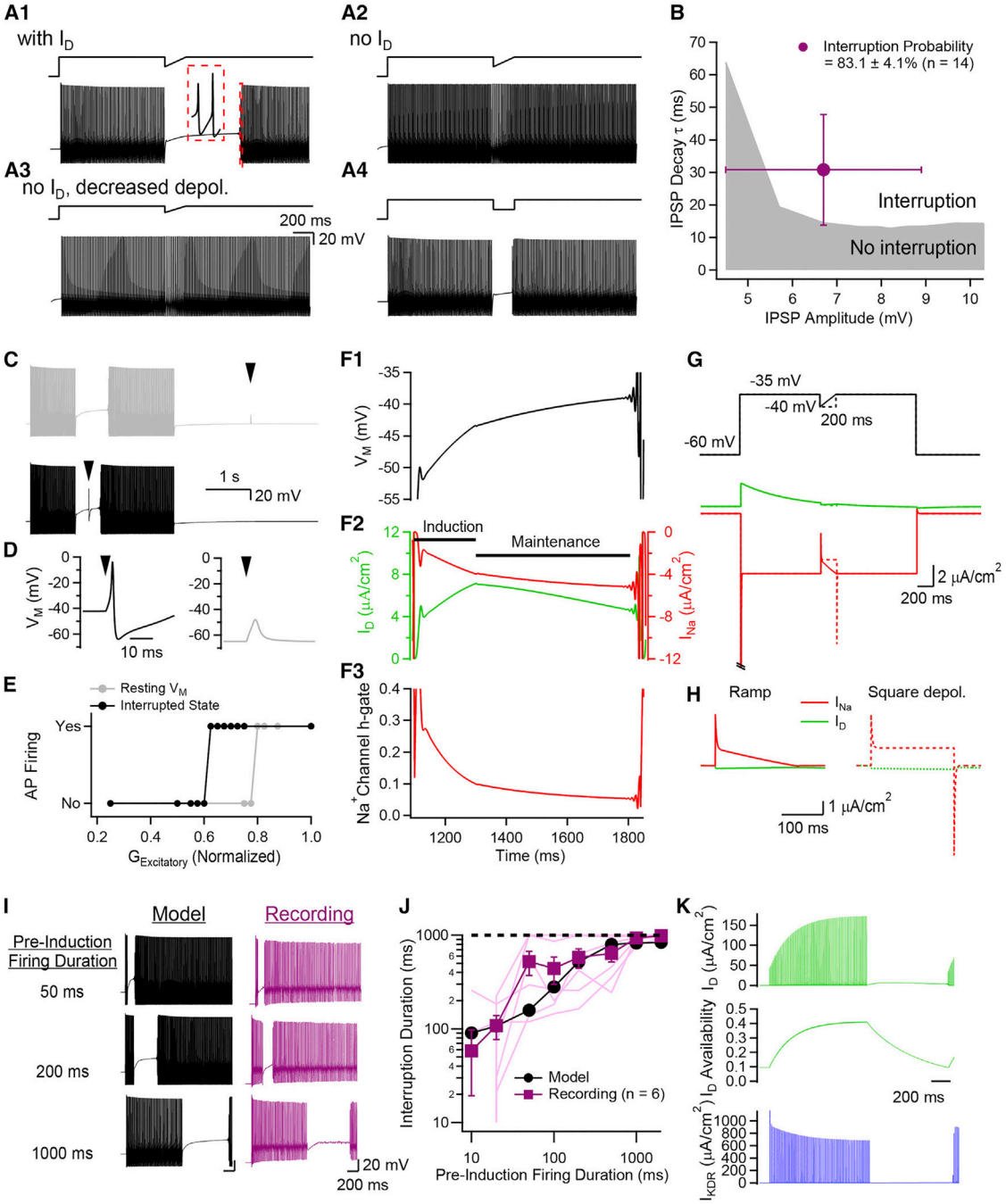


**Figure 7. A single-compartment conductance-based model reproduces core features of interruption**

(A) Model-generated firing patterns. Inset (A1), first two APs upon firing resumption.

(B) An inhibitory conductance in the model reliably interrupted firing. Model parameters comparable to experimentally measured IPSPs reliably generating interruptions (purple cross). Pre-interruption firing duration kept constant (1 s) across experimental and modeling conditions.

(C–E) (C) Model neuron is hypersensitive to excitatory inputs during the firing interruption. An excitatory conductance (arrowhead) was introduced at resting $V_M$ (gray) or during the

interruption (black). (D) At resting $V_M$, the excitatory conductance is subthreshold while the same conductance triggers an AP during interruption. (E) Quantification of excitatory strength required to generate AP, showing increased excitability in interrupted state.
(F) (F1) $V_M$ during interruption. (F2) $I_D$ and $I_{Na}$ dynamics during interruption. (F3) $Na^+$ channel inactivation variable (h-gate) during interruption.
(G and H) Voltage-clamping the model with $V_M$ dynamics known to interrupt neurons (full line) or to resume their firing (dotted line). $I_{Na}$ transient triggered by offset of rectangular hyperpolarization.
(I) Longer pre-induction bursts are associated with increased duration of interruption in simulations and experiments. Interruptions induced by an inhibitory conductance in model and a mock IPSC in experiments (as in Figure 4B).
(J) Interruption duration plateaued as pre-induction firing was prolonged in simulations and experiments (n = 6 neurons; p = 0.18; two-way ANOVA) due to saturating degree of removal of $I_D$ inactivation for longer firing episodes.
(K) Membrane current dynamics underlying the 1,000 ms pre-induction firing duration (I, bottom).

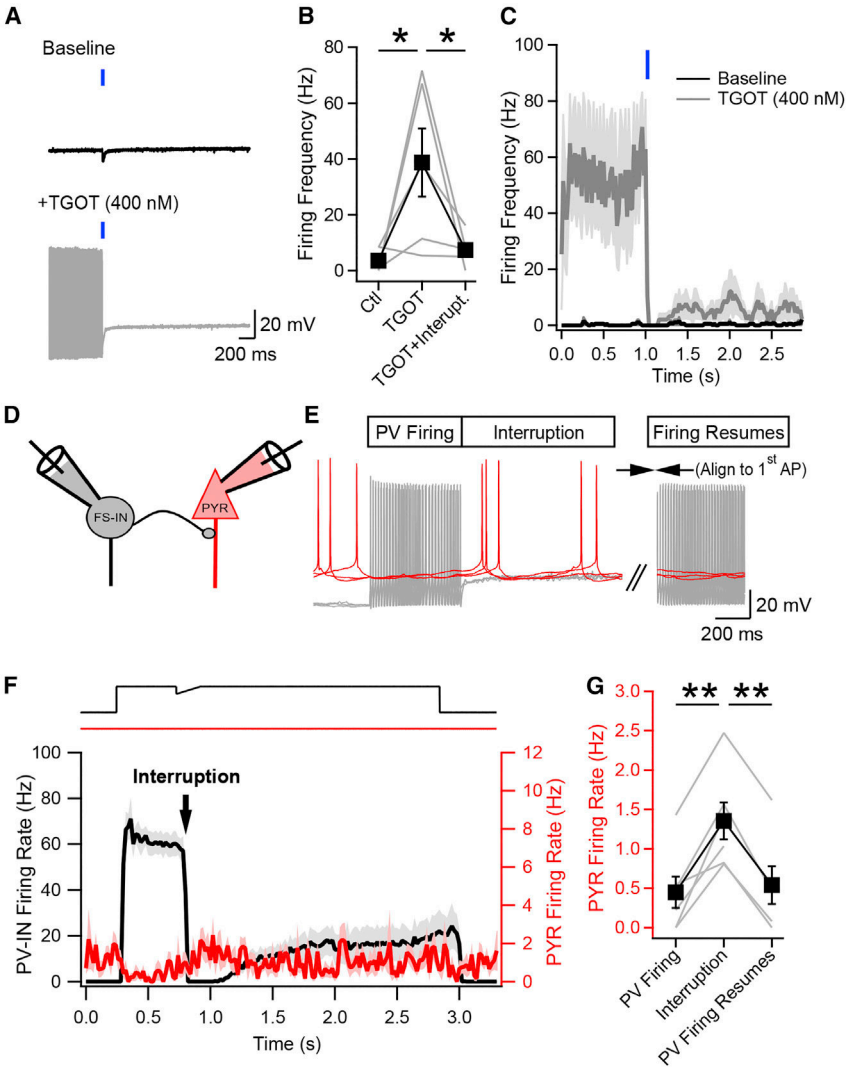


**Figure 8. The firing interruption is effective for oxytocin-induced PV-IN firing and disinhibits CA1 pyramidal neurons**

(A) Current-clamp recording from a PV-IN at baseline (top) and after TGOT (bottom). 10 traces each overlayed for baseline and TGOT.

(B) Pooled data (n = 5) showing effect of TGOT and further optogenetic activation of SST-INs.

(C) SST-IN-mediated synaptic inhibition persistently interrupts PV-INs driven to fire by OXTR activation (n = 4).

(D and E) Paired recording from a PV-IN (gray) synaptically connected to a CA1-PYR (red); 3 consecutive sweeps during interruption induced by mockIPSC as in (F).

(F) AP firing frequency for PV-INs (black) and CA1-PYRs (n = 6 pairs). Shaded areas, standard error.

(G) AP frequency recorded in the CA1-PYR for500 ms windows measured during PV-IN firing, at interruption onset (n = 6; **p < 0.01) and following PV-IN firing resumption (n

= 4; **p < 0.01; 2 PYRs excluded because resumption of PV-IN firing too rare to reliably assess PYR firing rate).

## KEY RESOURCES TABLE

| REAGENT or RESOURCE | SOURCE | IDENTIFIER |
|---|---|---|
| Antibodies | | |
| KV1.1 (KCNA1) Recombinant Rabbit Monoclonal Antibody (SN66-06) | ThermoFisher Scientific | Catalog no. MA5-32317; RRID: AB_2809599 |
| Alexa-633 conjugated streptavidin | ThermoFisher Scientific | Catalog no. S21375 |
| Chemicals, peptides, and recombinant proteins | | |
| Dendrotoxin-K | Alomone Labs | Catalog no. D-400; CAS no. 119128-61-9 |
| Dendrotoxin-I | Alomone Labs | Catalog no. D-390; CAS no. 107950-33-4 |
| (-)-Bicuculline methiodide | Tocris | Catalog no. 2503; CAS no. 40709-69-1 |
| Biocytin | Cayman Chemical Company | Catalog no. 16751; CAS no. 576-19-2 |
| Tetrodotoxin (citrate) | Cayman Chemical Company | Catalog no. 14964; CAS no. 18660-81-6 |
| CGP 55845 hydrochloride | Tocris | Catalog no. 1248/10; CAS no. 149184-22-5 |
| Pertussis toxin from *Bordetella pertussis* | Sigma-Aldrich | Catalog no. P7208; CAS no. 70323-44-3 |
| κ-Conotoxin RIIIK | Alomone Labs | Catalog no. STC-650 |
| Agitoxin-2 | Alomone Labs | Catalog no. STA-420; CAS no. 168147-41-9 |
| ($Thr^4$,$Gly^7$)-oxytocin (TGOT) | Bachem | Catalog no. 4013837.0025; CAS no. 60786-59-6 |
| Deposited data | | |
| *In vivo* electrophysiological data | Buzsaki Lab Databank | https://buzsakilab.com/wp/public-data/ |
| Experimental models: Organisms/strains | | |
| Mouse: B6;129P2-*Pvalb*$^{tm1(cre)Arbr}$/J | The Jackson Laboratory | Stock no. 008069; RRID: IMSR_JAX:008069 |
| Mouse: *Sst*$^{tm2.1(cre)Zjh}$/J | The Jackson Laboratory | Stock no. 013044; RRID: IMSR_JAX:013044 |
| Mouse: *Vip*$^{tm1(cre)Zjh}$/J | The Jackson Laboratory | Stock no. 010908; RRID: IMSR_JAX:010908 |
| Mouse: B6.Cg-*Gt(ROSA)26Sor*$^{tm9(CAG-tdTomato)Hze}$/J | The Jackson Laboratory | Stock no. 007909; RRID: IMSR_JAX:007909 |
| Mouse: B6.Cg-*Gt(ROSA)26Sor*$^{tm32(CAG-COP4*H134R/EYFP)Hze}$/J | The Jackson Laboratory | Stock no. 024109; RRID: IMSR_JAX:024109 |
| Software and algorithms | | |
| Clampfit | Molecular Devices | v10.3.2,1 |
| Clampex | Molecular Devices | v8.2 and v9.2 |
| Igor Pro | WaveMetrics | V6.3.7.2 |
| Neurolucida 360 | MBF Bioscience | V2.70.1 |
| HippoCookBook toolbox (MATLAB© toolbox for extracellular/intracellular recordings) | Manuel Valero | https://doi.org/10.5281/zenodo.6902376 |
| KiloSort (template-based spike sorting MATLAB© software) | Pachitariu & Cortex-lab | https://github.com/cortex-lab/KiloSort |
| KilosortWrapper | Peter C. Petersen & Brendon Watson | https://github.com/petersenpeter/KilosortWrapper |
| Phy (Python GUI for manual spike curation) | Cyrille Rossant, Ken. Harris et al. | https://github.com/cortex-lab/phy |

| REAGENT or RESOURCE | SOURCE | IDENTIFIER |
|---|---|---|
| Phy plugins | Peter C. Petersen | https://github.com/petersenpeter/phy1-plugins |
| MATLAB© | Mathworks | https://www.mathworks.com/ |
| CellExplorer (Cell classification pipeline and graphical interface) | Petersen and Buzsáki,[100] | https://linkinghub.elsevier.com/retrieve/pii/S0896627321006565 |